國立臺灣大學工學院工程科學及海洋工程學系

碩士論文

Department of Engineering Science and Ocean Engineering

College of Engineering

National Taiwan University

Master Thesis

應用契比雪夫配置法探討自由傳播波浪下黏性流

之穩定性分析

Stability Analysis of Viscous Flow beneath a Free-Propagating

Surface Wave Using Chebyshev Collocation Method

胡家宜

Chia-I Hu

指導教授：蔡武廷 博士

Advisor: Wu-Ting Tsai, Ph.D.

中華民國 107 年 1 月

January 2018

中文摘要

　　朗謬爾環流(Langmuir Circulation)係因海面波浪與風成流之交互作用形成，然於自由傳播波浪之數值模擬結果中，亦發現類似於朗謬爾環流之渦旋。本研究以 Craik-Leibovich equation 之線性穩定性分析，判斷 Craik-Leibovich type 2 (CL2)不穩定性能否解釋此現象。此穩定性分析以正規模態展開線性擾動方程式，並以契比雪夫配置法(Chebyshev Collocation Method)求解；契比雪夫配置法乃基於契比雪夫多項式、點配置法之擴展，及衍伸出的廣義特徵值之解。研究發現最不穩定模態與於數值模擬及實驗觀察之主要渦旋對間距相近；因此，被觀察到之條痕有很高可能性為 CL2 不穩定性所造成。

關鍵字：自由傳播波浪、朗謬爾環流、Craik-Leibovich equation、契比雪夫配置法、不穩定性

Abstract
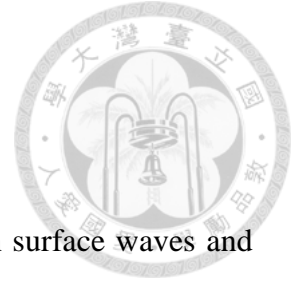
Langmuir circulations are formed from the interaction between surface waves and wind driven currents, however in the numerical simulations of free-propagating surface waves, streaks resembling the Langmuir circulation exists. Linear stability analysis of the Craik-Leibovich equation is conducted to determine if the Craik-Leibovich type 2 (CL2) instability can explain the similarities. The analysis is done by representing the perturbations by normal-mode expansion, and solved using Chebyshev collocation method; this method is based on expansions in terms of Chebyshev polynomials, point collocation, and subsequent solution of the generalized eigenvalue problem. The most unstable mode is found to be close to the spacing of predominant vortex pairs observed in numerical simulations and laboratory experiments; hence, it is highly probable that the elongated streaks observed on the surfaces are excited by the CL2 instability.
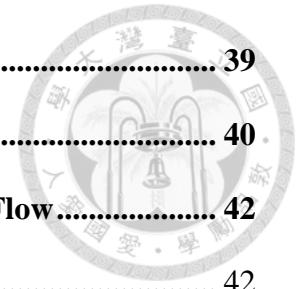
Keywords: free-propagating wave, Langmuir circulation, Craik-Leibovich equation, Chebyshev collocation method, instability

Contents

iv

List of Figures

List of Tables

List of Symbols

Greek Alphabet

β	Thermal expansion coefficient
ρ	Reference water density
σ	Surface wave frequency
τ	Shear stress induced by viscous action of waves
τ_w	Wind stress
θ	Temperature perturbation
Θ	Temperature
π	Pressure perturbation
Π	Modified pressure
α_T	Thermal diffusivity
ν_T	Eddy viscosity
λ	Surface wavelength
λ_d	Spanwise disturbance wavelength

English Alphabet

x	Streamwise axis
y	Spanwise axis
z	Vertical axis
u	Streamwise velocity
v	Spanwise velocity
w	Vertical velocity
a	Characteristic wave amplitude
c	Complex wave velocity
g	Acceleration due to gravity
k	Streamwise wavenumber
l	Nondimensional wavenumber
t	Time
U	Mean shear velocity
u_*	Water friction velocity

ix

u_s		Stokes drift velocity
$\overline{u_e}$		Eulerian mean flow
Ri		Richardson number
La		Langmuir number
Pr		Prandtl number
T_n		nth-degree Chebyshev polynomial of the first kind
N		Order of Chebyshev polynomial

Subscripts

$\hat{\cdot}$		Eigenfunction
$\tilde{\cdot}$		Dimensional

Chapter 1.   Introduction

1.1   *Langmuir Circulation beneath Wind Waves*

On the surface of the lakes or oceans, one can frequently observe streaks, or commonly called 'windrows', that aligns approximately with the wind direction; made visible by the collection of flotsam or foam, or the compression of organic film that concentrate in lines of surface convergence. This phenomenon was first documented by Langmuir (1938), who noticed the patterns of floating seaweed while crossing the Atlantic in 1927; hence bears the name 'Langmuir circulation'.

The Langmuir circulation are sets of vortices with axis parallel to the wind direction that occur on the upper layers of lakes and oceans. The theory describing these wind-driven convective motions has been offered by Craik & Leibovich (1976), known as the Craik-Leibovich equation (CL-equation); and are set out in their fullest form in Leibovich (1977*b*), for the Eulerian-mean flow of the ocean subject to surface waves and an applied wind stress. It was later proposed that the Langmuir circulation rises as an instability of these equations.

The CL-equation admit two types of instability mechanisms, Craik–Leibovich type 1 and 2 (CL1 and CL2), depending on the behavior of the drift. The latter is considered more relevant in the ocean and consequently most studied thus is the one considered in our current study. Leibovich & Paolucci (1981) studied the stability analysis of the CL-equation to two-dimensional disturbances, and found that the conditions typically occurring in the oceans are highly unstable to the CL2 instability.

1.2 *Vortical Flow beneath Free-Propagating Waves*

The Langmuir circulation is considered to be formed from the interaction of the Lagrangian drift of the surface waves and the mean shear current driven by the wind. Yet, in the numerical simulations of free-propagating (non-breaking) surface waves by Tsai *et al.* (2015) elongated surface streaks are also observed; since no imposed surface stress exists, supposedly there should not be an imposed shear. It has been a prevalent notion that the flow beneath such waves is essentially irrotational; but in fact, Longuet-Higgins (1953) established that the free-surface boundary condition guarantees the existence of a shear flow; accordingly, Craik (1982) reasoned that the free-surface boundary conditions generate a surface stress that successively produces a second-order Eulerian shear current. Therefore, the numerical simulations have both shear and drift, and are prone to the CL2 instability.

In the laboratory experiments by Savelyev *et al.* (2012) using thermal-marking velocimetry elongated thermal streaks in the direction of wave propagation similar to that of Langmuir circulations were also observed, suggesting the existence of streamwise vortices underneath the surface.

1.3 *Outline of this Thesis*
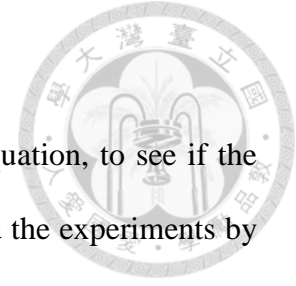
In this study, we conduct linear stability analysis of the CL-equation, to see if the vortices observed in numerical simulations by Tsai *et al*. (2015) and the experiments by Savelyev *et al*. (2012) can be explained by the CL2 instability. Though previously studied in Tsai *et al.* (2017), they had used the Galerkin method; we aim to revisit the case using Chebyshev collocation method.

We first begin by introducing the general set of the wave-averaged governing equations in 2.1; the nondimensionalizing is presented in 2.2. The linearized perturbed equation of the CL-equation is adapted to the case of free-propagating surface wave in 2.3. Chapter 3 goes through the numerical procedures of solving the linear stability analysis. By introducing the normal mode expansions in 3.1, the partial differential equations is reduced to a set of ordinary differential equation, which we solve by the Chebyshev collocation method described in 3.2, the validity of which is examined in 3.3. Results of the linear stability analysis are presented in Chapter 4. In 4.1 comparison of our analysis with the numerical simulation and laboratory experiments are made, some additional observations of the solutions are explored in 4.2 and 4.3, and the velocity profile corresponding to the most unstable mode is presented in 4.4. Conclusions on our current work are drawn in Chapter 5.

Chapter 2.   Problem Formulation

2.1   *Governing Equations*

First and foremost, we look at the CL-equations, these equations governing the Langmuir circulations were originally derived by Leibovich (1977*b*), here we follow the works of Lele (1985) on a generalized version. The Eulerian means for a fluid under the action of surface wind drift current is considered. Take the direction of wind stress as the positive $\tilde{x}$-coordinate (unit vector $\boldsymbol{i}$), let the mean free surface coincide with the $(\tilde{x}, \tilde{y})$ plane, and set $\tilde{z}$ positive vertically upwards (unit vector $\boldsymbol{k}$) from the mean free surface. The constant wind stress on the mean free surface is represented by τ_w, where u_* is the related water friction velocity and ρ is a reference water density. The surface wave has the characteristic frequency σ, wavenumber k, and amplitude a and also propagate in the wind direction. In the Boussinesq approximation, the motion of the Langmuir circulation currents is given by

$$\frac{\partial \widetilde{\boldsymbol{v}}}{\partial \tilde{t}} + \left(\widetilde{\boldsymbol{v}} \cdot \widetilde{\boldsymbol{\nabla}}\right)\widetilde{\boldsymbol{v}} = \widetilde{\boldsymbol{u}}_s \times \left(\widetilde{\boldsymbol{\nabla}} \times \widetilde{\boldsymbol{v}}\right) - \widetilde{\boldsymbol{\nabla}}\widetilde{\Pi} + \beta g \tilde{\Theta} \boldsymbol{k} + \nu_T \widetilde{\boldsymbol{\nabla}}^2 \widetilde{\boldsymbol{v}}, \tag{2.1}$$

$$\frac{\partial \tilde{\Theta}}{\partial \tilde{t}} + \left(\widetilde{\boldsymbol{v}} \cdot \widehat{\boldsymbol{\nabla}}\right)\tilde{\Theta} = \alpha_T \widetilde{\boldsymbol{\nabla}}^2 \tilde{\Theta}, \tag{2.2}$$

$$\widetilde{\boldsymbol{\nabla}} \cdot \widetilde{\boldsymbol{v}} = 0. \tag{2.3}$$

The superscript "wiggle" denotes dimensional quantities, while the bold symbol marks vector terms, and $\widetilde{\boldsymbol{\nabla}}$ is the dimensional del operator. Here $\widetilde{\boldsymbol{v}}$ represents the velocity, $\tilde{\Theta}$ is the temperature field, and $\widetilde{\Pi}$ is a modified pressure. The Stokes drift velocity $\widetilde{\boldsymbol{u}}_s$ arises from averaging the irrotational flow that corresponds to the surface gravity waves and varies with depth only for the CL2 mechanism (Leibovich 1983); although it is a Lagrangian concept, it arises in this model in a purely Eulerian framework propagating in the wave direction. g is the acceleration due to gravity in the $-\tilde{z}$ direction, β is the

4

thermal expansion coefficient, ν_T is an (assumed constant) eddy viscosity representing the turbulent diffusivity of momentum, and α_T is the thermal diffusivity. The parameters $\widetilde{\boldsymbol{u}}_s$, ν_T, and α_T are assumed to be constant in time.
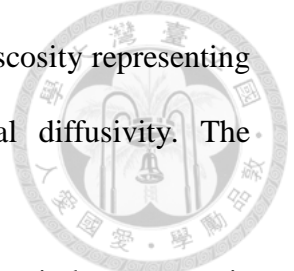
At the mean free surface the vertical current vanishes, and the wind stress τ_w is constant on the plane $z = 0$, with no component transverse to the wind direction, this leads to the boundary conditions

$$\widetilde{w} = \widetilde{\theta} = \frac{d\widetilde{v}}{d\widetilde{z}} = 0, \frac{d\widetilde{u}}{d\widetilde{z}} = \frac{\tau_w}{\rho \nu_T} \quad \text{on} \quad \widetilde{z} = 0, \tag{2.4}$$

and the boundary conditions at the infinite water depth are

$$\widetilde{\boldsymbol{v}} \to 0, \qquad \widetilde{\theta} \to 0 \quad \text{as} \quad \widetilde{z} \to -\infty. \tag{2.5}$$

The problem is complete with these boundary conditions; in the next section, we will proceed with nondimensionalizing the governing equations (2.1)-(2.3).

5

2.2 *Nondimensional Governing Equations*
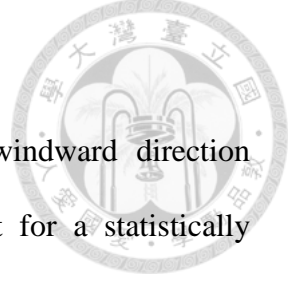
Under the assumption that the system is uniform in the windward direction ($\tilde{x}$-direction), and that the water mass is initially at rest, except for a statistically stationary random surface wave field propagating in the wind direction, we write

$$\tilde{\boldsymbol{v}} = \tilde{\boldsymbol{v}}(\tilde{y}, \tilde{z}, \tilde{t}) = (\tilde{u}, \tilde{v}, \tilde{w}), \tag{2.6}$$

$$\tilde{\Theta} = \tilde{T}_c(\tilde{z}, \tilde{t}) + \tilde{\theta}(\tilde{y}, \tilde{z}, \tilde{t}), \tag{2.7}$$

$$\tilde{\boldsymbol{u}}_s = (\tilde{u}_s(\tilde{z}), 0, 0), \tag{2.8}$$

$$\tilde{\Pi} \equiv \tilde{\Pi}_c(\tilde{z}, \tilde{t}) + \tilde{\pi}(\tilde{y}, \tilde{z}, \tilde{t}), \tag{2.9}$$

here $\tilde{T}_c$ is the conduction solution (in a motionless fluid), with suitable boundary conditions; also, a perturbation $\tilde{\pi}$ is introduced to the modified pressure $\tilde{\Pi}$, where

$$-\frac{\partial \tilde{\Pi}_c}{\partial \hat{t}} + \beta g \tilde{T}_c = 0. \tag{2.10}$$

While the CL-equations can be nondimensionalized in many ways, we follow Leibovich & Paolucci (1981), taking the characteristic quantities of length, time, and velocities as:

$$\mathcal{L} = k^{-1}, \tag{2.11}$$

$$\mathcal{T} = \frac{1}{aku_*}\left(\frac{\nu_T}{\sigma}\right)^{\frac{1}{2}}, \tag{2.12}$$

$$\mathcal{U} = \left(\frac{u_*^2}{\nu_T k}\right), \tag{2.13}$$

$$\mathcal{V} = u_* a \left(\frac{\sigma}{\nu_T}\right)^{\frac{1}{2}}, \tag{2.14}$$

$$\mathcal{U}_S \equiv a^2 k \sigma, \tag{2.15}$$

where the wave angular frequency $\sigma = (gk)^{1/2}$. Set dimensionless variables as:

$$(\tilde{x}, \tilde{y}, \tilde{z}) = [\mathcal{L}](x, y, z), \tag{2.16}$$

6

$$\tilde{t} = [\mathcal{T}]t, \tag{2.17}$$

$$\tilde{u}_s(\tilde{z}) = [\mathcal{U}_S]u_s(z), \tag{2.18}$$

$$\tilde{\Pi} = [\mathcal{V}]^2\Pi, \tag{2.19}$$

$$\tilde{u} = [\mathcal{U}]u, \qquad \tilde{v} = [\mathcal{V}]v, \qquad \tilde{w} = [\mathcal{V}]w, \tag{2.20}$$

$$\tilde{\theta} = [k^{-1}T'_\infty]\theta, \tag{2.21}$$

where T'_∞ is a scale of temperature gradient taken to be in the abyss. The variables are nondimensionalized with the bracketed scales, note that the streamwise velocity component is nondimensionalized by $\mathcal{U}$, while the spanwise and vertical velocities are scaled by $\mathcal{V}$.

Introduce the definitions (2.6)-(2.10), where the quantities $\tilde{T}_c$ and $\tilde{\Pi}_c$ themselves satisfy (2.1)-(2.2), and the dimensionless variables (2.16)-(2.21) into the general equations (2.1)-(2.3). For (2.1) we obtain

$$\frac{\partial u}{\partial t} + \left(v\frac{\partial u}{\partial y} + w\frac{\partial u}{\partial z}\right) = La\left(\frac{\partial^2 u}{\partial y^2} + \frac{\partial^2 u}{\partial z^2}\right), \tag{2.22}$$

$$\frac{\partial v}{\partial t} + \left(v\frac{\partial v}{\partial y} + w\frac{\partial v}{\partial z}\right) = u_s\frac{\partial u}{\partial y} - \frac{\partial \pi}{\partial y} + La\left(\frac{\partial^2 v}{\partial y^2} + \frac{\partial^2 v}{\partial z^2}\right), \tag{2.23}$$

$$\frac{\partial w}{\partial t} + \left(v\frac{\partial w}{\partial y} + w\frac{\partial w}{\partial z}\right) = u_s\frac{\partial u}{\partial z} - \frac{\partial \pi}{\partial z} + Ri\theta + La\left(\frac{\partial^2 w}{\partial y^2} + \frac{\partial^2 w}{\partial z^2}\right), \tag{2.24}$$

The full set of nondimensional governing equations are then

$$\frac{\partial \boldsymbol{v}}{\partial t} + (\boldsymbol{v} \cdot \boldsymbol{\nabla}_p)\boldsymbol{v} = u_s\boldsymbol{\nabla}_p u + Ri\theta\boldsymbol{k} - \boldsymbol{\nabla}_p\pi + La\boldsymbol{\nabla}_p^2\boldsymbol{v}, \tag{2.25}$$

$$\frac{\partial \theta}{\partial t} + (\boldsymbol{v} \cdot \boldsymbol{\nabla}_p)\theta = -w\phi + LaPr^{-1}\boldsymbol{\nabla}_p^{\;2}\theta, \tag{2.26}$$

$$\boldsymbol{\nabla}_p \cdot \boldsymbol{v} = 0, \tag{2.27}$$

where $\phi \equiv \partial T_c/\partial z$, and the operator $\boldsymbol{\nabla}_p \equiv \frac{\partial}{\partial y}\boldsymbol{j} + \frac{\partial}{\partial z}\boldsymbol{k}$ is defined for convenience.

The arising dimensionless parameters from the nondimensional governing equations (2.25)-(2.27) are

7

$$La \equiv \frac{k\nu_T}{au_*}\left(\frac{\nu_T}{\sigma}\right)^{\frac{1}{2}}, \tag{2.28}$$

$$Ri \equiv \frac{\beta g T'_\infty}{(au_* k)^2}\frac{\nu_T}{\sigma}, \tag{2.29}$$

$$Pr \equiv \frac{\nu_T}{\alpha_T}, \tag{2.30}$$

where La is the Langmuir number introduced by Leibovich (1977a). The parameter Ri plays a role of an overall Richardson number, providing a measure of the relative importance of the buoyancy and inertia forces. The (turbulent) Prandtl number, Pr, represents the relative rates of (turbulent) diffusion of momentum and heat. Furthermore, for linear thermocline, it follows that $\phi(z,t) = 1$, then (2.25)-(2.27) is identical to the dimensionless governing equations studied in Leibovich & Paolucci (1981).

8

2.3   *Linearized Perturbed Equation*

To study the stability of the perturbed velocity based on the nondimensional CL-equations (2.25)-(2.26), we construct stability analysis by superimposing a disturbance to the one-dimensional base state, which is assumed to be quasi-steady, i.e. independent of time. Decomposing the velocity into a mean and its perturbation:

$$u(y, z, t) \equiv U(z) + u'(y, z, t), \tag{2.31}$$

$$v(y, z, t) \equiv 0 + v'(y, z, t), \tag{2.32}$$

$$w(y, z, t) \equiv 0 + w'(y, z, t), \tag{2.33}$$

where $\boldsymbol{v}' = (u', v', w')$ is the streamwise-averaged Eulerian velocity perturbations, and the mean shear velocity U induced by the wind is time-independent and only differs in the vertical direction.

We consider the linear stability by assuming that the disturbance velocity $\boldsymbol{v}'$, modified pressure π, and temperature deviation from conduction θ are infinitesimally small, so that the nonlinear terms on the left-hand side of equations (2.25) and (2.26) may be neglected. Since all velocities dealt with beyond this point are the perturbed velocities, for better readability, we lose the prime notation; all perturbed velocities $\boldsymbol{v}' = (u', v', w')$ will henceforth be termed as $\boldsymbol{v} = (u, v, w)$. Noting that the mean flow satisfies (2.25)-(2.27), the linearized equations of the perturbed velocities results in

$$\frac{\partial u}{\partial t} = -w \frac{\partial U}{\partial z} + La \left(\frac{\partial^2 u}{\partial y^2} + \frac{\partial^2 u}{\partial z^2} \right), \tag{2.34}$$

$$\frac{\partial v}{\partial t} = u_s \frac{\partial u}{\partial y} - \frac{\partial \pi}{\partial y} + La \left(\frac{\partial^2 v}{\partial y^2} + \frac{\partial^2 v}{\partial z^2} \right), \tag{2.35}$$

$$\frac{\partial w}{\partial t} = u_s \frac{\partial u}{\partial z} - \frac{\partial \pi}{\partial z} + Ri\theta + La \left(\frac{\partial^2 w}{\partial y^2} + \frac{\partial^2 w}{\partial z^2} \right), \tag{2.36}$$

represented in vector form

9

$$\frac{\partial \boldsymbol{v}}{\partial t} = u_s \boldsymbol{\nabla}_p u - w \frac{\partial U}{\partial z} \boldsymbol{i} - \boldsymbol{\nabla}_p \pi + Ri\theta \boldsymbol{k} + La\boldsymbol{\nabla}_p^2 \boldsymbol{v}. \tag{2.37}$$

The linearized perturbed equations is then (2.37) along with

$$\frac{\partial \theta}{\partial t} = -w + LaPr^{-1}\boldsymbol{\nabla}_p{}^2\theta, \tag{2.38}$$

$$\boldsymbol{\nabla}_p \cdot \boldsymbol{v} = 0, \tag{2.39}$$

where the dimensionless Stokes drift for deep water is

$$\boldsymbol{u_s} = u_s \boldsymbol{i} = e^{2z}\boldsymbol{i}. \tag{2.40}$$

At the mean free surface the vertical current vanishes, and the wind stress τ_w is constant on the plane $z = 0$, with no component transverse to the wind direction, this leads to the boundary conditions of the perturbed quantities as

$$w = \theta = \mathcal{D}v = \mathcal{D}u = 0 \quad \text{on} \quad z = 0, \tag{2.41}$$

the boundary conditions at the infinite water depth are

$$\boldsymbol{v} \to 0, \quad \theta \to 0 \quad \text{as} \quad z \to -\infty, \tag{2.42}$$
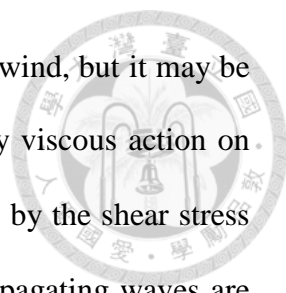
where the operator $\mathcal{D} \equiv \partial/\partial z$. In the above work, the mean shear velocity U was regarded as derived from an applied wind stress.

Now considering the free propagating periodic wave, according to potential theory, there exists a second-order mean Lagrangian drift, which is the Stokes drift $\boldsymbol{u_s}$ mentioned before. In the absence of wind, no shear stress acts upon the water surface; such flow was thought to be irrotational. However, Longuet-Higgins (1953) recognized that a second-order Eulerian drift current $\overline{u_e}$ is caused by the viscous action of the waves. The induced second-order shear stress

$$\tau = 2\rho\nu\sigma(ak)^2, \tag{2.43}$$

acts on the edge of the boundary layer and is equivalent to a wave stress acting on the surface, which gives rise to the existence of a shear flow $\overline{u_e}$ in the direction of wave propagation, the dimensionless mean shear velocity gradient is $\mathcal{D}\overline{u_e} = 1$. In the works

10

of Leibovich & Paolucci (1981) they had regarded the stress due to wind, but it may be readily attributed to the free-surface boundary condition induced by viscous action on the waves; the results remain valid on replacing the wind stress τ_w by the shear stress τ (Craik 1982). Our linearized perturbed equations for the free propagating waves are then the set (2.37)-(2.39) with the mean shear velocity U arising from the wind now replaced with the mean Eulerian current $\overline{u_e}$.

In our current study the temperature is treated as a passive tracer, we consider the temporal instability in the absence of density stratification; neglecting the buoyancy effect, we let $Ri = 0$. In this limit, the equation governing the temperature perturbation decouples from equation (2.37) and has no effect on the stability characteristics, and the value of Pr can be arbitrary.

Chapter 3. Numerical Procedure of Linear Stability Analysis

3.1   *Normal Mode Expansion*

For linear instability, the arbitrary disturbance can be decomposed into a complete set of normal modes, the linearity implies that the various modes do not interact, and the stability of each mode is examined separately. Considering the temporal instability

$$(\boldsymbol{v}, \pi, \theta) = \mathrm{Re}\{[\hat{\boldsymbol{v}}(y, z), \hat{\pi}(y, z), \hat{\theta}(y, z)]e^{st}\}, \tag{3.1}$$

where $\hat{\boldsymbol{v}}, \hat{\pi}, \hat{\theta}$ are complex, and the growth rate is the real part of s; being unstable if $\mathrm{Re}(s) > 0$, stable if $\mathrm{Re}(s) < 0$, and neutrally stable for $\mathrm{Re}(s) = 0$. In the following context, the real part of the growth rate $\mathrm{Re}(s)$ will be represented by s_r, while the imaginary part will be s_i. Transverse instability of the flow is sought for by assuming the spanwise periodic disturbance with wavenumber l, consequently we write

$$(\boldsymbol{v}, \pi, \theta) = \mathrm{Re}\{[\hat{\boldsymbol{v}}(z), \hat{\pi}(z), \hat{\theta}(z)]e^{ily+st}\}, \tag{3.2}$$

where i is the imaginary unit, and $\hat{\boldsymbol{v}}, \hat{\pi}, \hat{\theta}$ are complex amplitudes; for an unstable mode, the amplitude of the disturbance will grow exponentially with time. Another common equivalent form is $(\boldsymbol{v}, \pi, \theta) = \mathrm{Re}\{[\hat{\boldsymbol{v}}(z), \hat{\pi}(z), \hat{\theta}(z)]e^{il(y-ct)}\}$, where l is a real wavenumber, and c is the complex wave velocity. The real part of c is the phase velocity of the wave, while the imaginary part of lc represents the growth rate, (unstable if $\mathrm{Im}(lc) > 0$).

For numerical purpose, we will map the semi-infinite domain to the finite plane with the transform

$$\zeta = e^z. \tag{3.3}$$

On solving the set (2.37)-(2.39), we reduce the number of equations from 5 to 3 by eliminating π with cross-differentiation, and replacing v by w with the continuity

12

equation. Inserting (3.2) into the result, we gain the fourth order ordinary differential equations

$$s\hat{u}(\zeta) = -(\mathcal{D}\overline{u_e})\hat{w}(\zeta) + La(\mathcal{M} - l^2)\hat{u}(\zeta),\tag{3.4}$$

$$s(\mathcal{M} - l^2)\hat{w}(\zeta) = l^2(\mathcal{D}u_s)\hat{u}(\zeta) + La(\mathcal{M} - l^2)^2\hat{w}(\zeta) - l^2 Ri\hat{\theta}(\zeta),\tag{3.5}$$

$$s\hat{\theta}(\zeta) = -\hat{w}(\zeta) + LaPr^{-1}(\mathcal{M} - l^2)\hat{\theta}(\zeta),\tag{3.6}$$

where we have set the operator $\mathcal{M}$ as:

$$\mathcal{M} \equiv \zeta\frac{d}{d\zeta}\left(\zeta\frac{d}{d\zeta}\right).\tag{3.7}$$

Since an arbitrary function can be represented via infinite series, we approximate $\hat{u}, \hat{w}$, and $\hat{\theta}$ by the generalized series:

$$\hat{u}(\zeta) = \sum_{n=0}^{\infty} a_n u_n(\zeta), \qquad \hat{w}(\zeta) = \sum_{n=0}^{\infty} b_n w_n(\zeta),$$

$$\hat{\theta}(\zeta) = \sum_{n=0}^{\infty} c_n \theta_n(\zeta),\tag{3.8}$$

where a_n, b_n, and c_n are coefficients, and the base functions u_n, w_n and θ_n are orthogonal functions on the interval $0 \leq \zeta \leq 1$.

Note that the boundary conditions (2.41) and (2.42) after the coordinate transform (3.3) and the expansion (3.8) had become

$$\hat{w} = \hat{\theta} = \mathcal{M}\hat{w} = \zeta\frac{d\hat{u}}{d\zeta} = 0 \quad \text{on} \ \ \zeta = 1,\tag{3.9}$$

$$\hat{u} = \frac{d\hat{w}}{d\zeta} = \hat{w} = \hat{\theta} = 0 \quad \text{on} \ \ \zeta = 0,\tag{3.10}$$

where we have interchanged the boundary conditions of v by w by means of the continuity equation.

Several methods could be used to solve the set of ordinary differential equations; two common methods are the Galerkin method and the collocation method. The main

13

difference between the two lies in that the Galerkin method make use of inner product while collocation method is of interpolation.

The Galerkin method had been used in Leibovich & Paolucci (1981), Phillips (2001), Phillips & Dai (2014), and Tsai *et al.* (2017), it involves integration, the mathematical procedure being more complicated thereupon more difficult to program. The formulation of Chebyshev collocation method is relatively easier, and had been used in Bookamp *et al.* (1997) for solving two-phase flow instability. Here we will use the Chebyshev collocation method to solve (3.4)-(3.6), and see if this simpler method can appropriately solve for the same stability analysis shown in Tsai *et al.* (2017).

3.2   *Chebyshev Collocation Method*
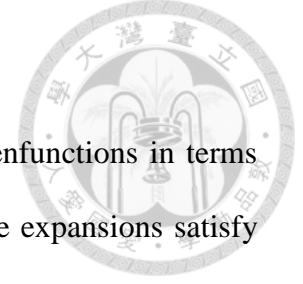
Chebyshev collocation method is based on expanding the eigenfunctions in terms of Chebyshev polynomials, and is characterized by the fact that the expansions satisfy the governing equations at every collocation point. The collocation points are a special set of optimal points in $[-1,1]$, known as Gauss-Lobatto grids which will soon be introduced below.

Chebyshev polynomials are orthogonal on the interval $[-1,1]$; to expand the eigenfunctions in terms of Chebyshev polynomials, we transform the equations (3.4)-(3.6) from the interval $[1,0]$ to $[-1,1]$ by a change of the independent variable ζ, achieved by means of the linear transformation

$$z_c = 2\zeta - 1. \tag{3.11}$$

We then approximate the eigenfunctions $\hat{u}(z_c), \hat{w}(z_c)$, and $\hat{\theta}(z_c)$ by the truncated (continuous) Chebyshev expansions

$$\hat{u}(z_c) = \sum_{n=0}^{N} a_n T_n(z_c), \qquad \hat{w}(z_c) = \sum_{n=0}^{N} b_n T_n(z_c),$$

$$\hat{\theta}(z_c) = \sum_{n=0}^{N} c_n T_n(z_c), \tag{3.12}$$

where $T_n(z_c)$ is the nth-degree Chebyshev polynomial of the first kind, defined by $T_n(z_c) = \cos(n \cos^{-1} z_c)$, for all non-negative integers n; and N is order of the polynomial that we truncated to. Derivatives of the eigenfunctions can be determined by differentiating the Chebyshev polynomials in (3.12), note that it is infinitely differentiable. Once transformed to the interval $[-1,1]$, we discretize by collocating the approximations (3.12) at the Gauss-Lobatto collocation points

$$z_{c_j} = \cos\frac{j\pi}{N}, \qquad j = 1,2,\dots N-1, \tag{3.13}$$

15

these are the extrema of the Chebyshev polynomials, where it has the unique property that all values of $T_n\left(z_{c_j}\right)$ are either 1 or -1. The eight boundary conditions on $z_c = 1$ $(j = 0)$ and $z_c = -1$ $(j = \mathrm{N})$ give the remaining equations that are required. More specifically, substitutions of the expansions (3.12) at the collocation points (3.13) into (3.4)-(3.6) gives $3(N - 1)$ equations in terms of the coefficients a_n, b_n, and c_n; while the eight boundary conditions gives another eight equations. Furthermore, to avoid dealing with the fourth order differential term in (3.5), we define

$$\hat{Y}(z_c) \equiv (\mathcal{M} - l^2)\hat{w}(z_c), \tag{3.14}$$

thus reducing equations (3.4)-(3.6) to a set of second order differential equations:

$$s\hat{u}(z_c) = -(\mathcal{D}\overline{u_e})\hat{w}(z_c) + La(\mathcal{M} - l^2)\hat{u}(z_c), \tag{3.15}$$

$$s(\mathcal{M} - l^2)\hat{w}(z_c) = l^2(\mathcal{D}u_s)\hat{u}(z_c) + La(\mathcal{M} - l^2)\widehat{Y}(z_c) - l^2Ri\hat{\theta}(z_c), \tag{3.16}$$

$$s\hat{\theta}(z_c) = -\hat{w}(z_c) + LaPr^{-1}(\mathcal{M} - l^2)\hat{\theta}(z_c), \tag{3.17}$$

$$(\mathcal{M} - l^2)\hat{w}(z_c) - \hat{Y}(z_c) = 0. \tag{3.18}$$

Analogous to (3.12), we expand $\hat{Y}$ as:

$$\hat{Y}(z_c) = \sum_{n=0}^{N} d_n T_n(z_c). \tag{3.19}$$

This system of equations gives $4(N - 1)$ equations, along with the eight boundary conditions

$$\hat{w} = \hat{\theta} = \mathcal{M}\hat{w} = \frac{d\hat{u}}{dz_c} = 0 \quad \text{on } z_c = 1, \tag{3.20}$$

$$\hat{u} = \frac{d\hat{w}}{dz_c} = \hat{w} = \hat{\theta} = 0 \quad \text{on } z_c = -1, \tag{3.21}$$

together forming the generalized eigenvalue problem

$$[A]\boldsymbol{a} = s[B]\boldsymbol{a}, \tag{3.22}$$

16

where s is the complex eigenvalue and $\boldsymbol{a}$ is the complex eigenvector of unknown coefficients $\boldsymbol{a}^{\mathrm{T}} = [a_0, a_1, \ldots, a_N, b_0, b_1, \ldots, b_N, c_0, c_1, \ldots, c_N, d_0, d_1, \ldots, d_N]$; there are a total of $4(N+1)$ equations and equal amount of unknowns, which can be solved using QZ-algorithms, we use the LAPACK subroutine ZGGEV3. The elements of matrix $[A]$ and $[B]$ are complex, their detailed formation can be found in Appendix B.1.

The matrix $[B]$ is singular, since the $\hat{Y}$ elements and the boundary conditions does not contain the eigenvalue s, more precisely, there are a total of $4N + 4$ equations with only $3N - 3$ equations that contain the eigenvalue s, resulting in $N + 7$ rows in $[B]$ that are zero. Due to these rows, the matrix will give $N + 7$ infinite eigenvalues (of large positive real part), which will interfere with finding the finite eigenvalues, these spurious eigenvalues are filtered out after our computation.
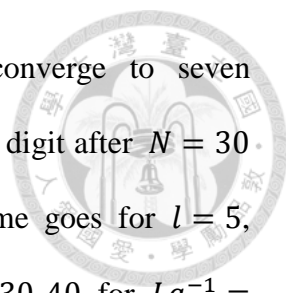
3.3   *Convergence Test of the Eigensystem*
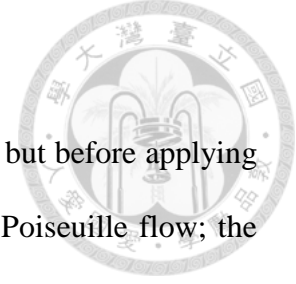
Validation of the Chebyshev collocation method must be made, but before applying to the CL-equation, first test on the stability analysis of the plane Poiseuille flow; the case is commonly used as reference to verify numerical methods for solving the linear stability analysis. Orszag (1971) implemented spectral method using expansions in Chebyshev polynomials and solved using Galerkin-Tau method. For the plane Poiseuille flow with the Reynolds number $Re = 10000$ and nondimensional wavenumber $k = 1$, the eigenvalue was found to be $0.23752649 + 0.00373967i$.

For the Chebyshev collocation method under the same parameters as with Orszag (1971), the eigenvalue solved using different order N is as shown in Table 1, where the eigenvalue is c from the form $e^{ik(x-ct)}$, detailed formulation and steps of the linear stability analysis for the plane Poiseuille flow are provided in Appendix A. From Table 1 we can see that the eigenvalue converges as the order of the Chebyshev polynomial increases; and is accurate to four significant digits at $N = 40$, while gradually converging (to eight significant digits) after $N = 60$, where the value converge to that of Orszag (1971). We conclude that the Chebyshev collocation method is indeed correct and proceed with solving the CL2 instability.

To check the accuracy of our results and also determine the order of Chebyshev polynomial needed for our analysis, we look into the convergence properties of our numerical method. The eigenvalue with the largest real part, s_r, indicating the most unstable mode, is of primary interest. Convergence of this eigenvalue is tested for various sets of reciprocal Langmuir number La^{-1} and nondimensional wavenumber l; we have picked five sets of wavenumber $l = 10.0, 5.0, 1.0, 0.5, 0.1$ with $La^{-1} = 100$, $1000, 10000$ respectively, the corresponding results are shown in Table 2-6 (where we have considered values of $|s_i| < 10^{-8}$ as zero).

For the set $l = 10$, at $La^{-1} = 10000$ the eigenvalues converge to seven significant digit after $N = 40$, while converging to eight significant digit after $N = 30$ for $La^{-1} = 1000$ and $N = 20$ for $La^{-1} = 100$. Roughly the same goes for $l = 5$, with eigenvalue converging to eight significant digits after $N = 20, 30, 40$ for $La^{-1} = 100, 1000, 10000$ respectively. For $l = 1$ the eigenvalues converge after $N = 20$ for $La^{-1} = 100, 1000$ and converges after $N = 30$ for $La^{-1} = 10000$.

For the lower wavenumbers, at $l = 0.1$ the eigenvalues did not converge even with increased amount of modes $N = 100$, in the case of $l = 0.5$ the convergence is still poor albeit slightly better for increased La^{-1}. From these results, we can tell that most eigenvalues converge with approximately $N = 20 \sim 40$; though for the lower wavenumbers l and lower reciprocal Langmuir numbers La^{-1}, the convergence properties are not desirable, especially in the lower wavenumber regions ($l < 1.0$) where the eigenvalues hardly converge.

The nondimensional spanwise wavenumber l is equivalent to the ratio of the surface wave wavelength $\lambda = 2\pi/k$ to the spanwise disturbance wavelength λ_d, i.e. $l = \lambda/\lambda_d$; the lower wavenumbers represents spanwise disturbance waves with longer wavelength relative to the surface wave length. Thus the range for $l < 1.0$ are of an extreme case representing large wavelength in the spanwise direction. We will overlook this zone since our main interest does not lay in this limited range; hence, we will select $N = 30$ for our computation, but keep in mind that the solutions corresponding to very low wavenumbers are not accurate. Eigenvalue comparisons with solutions using Galerkin method are provided in Appendix C.1

N	Eigenvalue c
20	$0.23803707 + 0.00588232i$
30	$0.23759437 + 0.00380300i$
40	$0.23752492 + 0.00373909i$
50	$0.23752652 + 0.00373958i$
55	$0.23752648 + 0.00373968i$
60	$0.23752649 + 0.00373967i$
65	$0.23752649 + 0.00373967i$
70	$0.23752649 + 0.00373967i$
Orszag (1971)	$0.23752649 + 0.00373967i$

TABLE 1. Convergence of eigenvalues using Chebyshev collocation method for the most unstable mode of plane Poiseuille flow for $k = 1, Re = 10000$.

10.0	$La^{-1} = 100$		$La^{-1} = 1000$		$La^{-1} = 10000$	
N	s_r	s_i	s_r	s_i	s_r	s_i
10	-0.00001002	0.0	0.84786810	0.0	0.96317802	0.0
20	-0.00001001	0.0	0.84980098	0.0	0.96360853	0.0
30	-0.00001001	0.0	0.84980121	0.0	0.96363626	0.0
40	-0.00001001	0.0	0.84980121	0.0	0.96363688	0.0
50	-0.00001001	0.0	0.84980121	0.0	0.96363689	0.0
100	-0.00001001	0.0	0.84980121	0.0	0.96363688	0.0

TABLE 2. Convergence of the real and imaginary parts of the eigenvalue s for the most unstable mode for $l = 10.0, La^{-1} = 100, 1000, 10000$.

5.0	$La^{-1} = 100$		$La^{-1} = 1000$		$La^{-1} = 10000$	
N	s_r	s_i	s_r	s_i	s_r	s_i
10	0.47014230	0.0	0.76723247	0.0	0.80203848	0.0
20	0.47053338	0.0	0.76757532	0.0	0.80206207	0.0
30	0.47053338	0.0	0.76757535	0.0	0.80207089	0.0
40	0.47053338	0.0	0.76757535	0.0	0.80207101	0.0
50	0.47053338	0.0	0.76757535	0.0	0.80207101	0.0
100	0.47053338	0.0	0.76757535	0.0	0.80207101	0.0

TABLE 3. Convergence of the real and imaginary parts of the eigenvalue s for the most unstable mode for $l = 5.0, La^{-1} = 100, 1000, 10000$.

1.0	$La^{-1} = 100$		$La^{-1} = 1000$		$La^{-1} = 10000$	
N	s_r	s_i	s_r	s_i	s_r	s_i
10	0.33765861	0.0	0.36486210	0.0	0.36860597	0.0
20	0.33766195	0.0	0.36490698	0.0	0.36861602	0.0
30	0.33766196	0.0	0.36490698	0.0	0.36861658	0.0
40	0.33766196	0.0	0.36490698	0.0	0.36861658	0.0
50	0.33766196	0.0	0.36490698	0.0	0.36861658	0.0
100	0.33766195	0.0	0.36490698	0.0	0.36861658	0.0

TABLE 4. Convergence of the real and imaginary parts of the eigenvalue s for the most unstable mode for $l = 1.0, La^{-1} = 100, 1000, 10000$.

0.5	$La^{-1} = 100$		$La^{-1} = 1000$		$La^{-1} = 10000$	
N	s_r	s_i	s_r	s_i	s_r	s_i
10	0.12739240	0.02386563	0.21644270	0.0	0.22376280	0.0
20	0.11704900	−0.06986582	0.20964760	0.0	0.22353840	0.0
30	0.10676850	−0.08969402	0.20219900	0.0	0.22289850	0.0
40	0.09737018	−0.10200260	0.19376530	0.0	0.22225120	0.0
50	0.08894719	0.11026750	0.18341190	0.0	0.22159950	0.0
100	0.05938821	0.12636050	0.15515550	−0.04275901	0.21827500	0.0

TABLE 5. Convergence of the real and imaginary parts of the eigenvalue s for the most unstable mode for $l = 0.5, La^{-1} = 100, 1000, 10000$.

0.1	$La^{-1} = 100$		$La^{-1} = 1000$		$La^{-1} = 10000$	
N	s_r	s_i	s_r	s_i	s_r	s_i
10	0.00188542	−0.02293515	0.03068427	0.01189717	0.05029377	0.0
20	−0.00000002	0.0	0.02276234	0.02351879	0.04525091	0.0
30	−0.00000001	0.0	0.01598400	0.02634776	0.03600912	0.00785463
40	−0.00000002	0.0	0.01172194	−0.02642398	0.03423464	−0.01392731
50	−0.00000001	0.0	0.00915277	0.02585865	0.03214168	0.01787070
100	0.00000002	0.0	0.00473512	−0.02358205	0.02143902	−0.02560851

TABLE 6. Convergence of the real and imaginary parts of the eigenvalue s for the most unstable mode for $l = 0.1, La^{-1} = 100, 1000, 10000$.

21

Chapter 4.   Results and Discussion

4.1   *Marginal Stability Curve & Stability Diagram*

Linear stability of the basic flow rests upon the stability of the set of ordinary differential equations (3.22). By stability, we mean that all solutions are bounded for all t; and the solution is unstable if it is unbounded for some $t > 0$, that is, if the solution of one mode is unstable ($s_r > 0$) the disturbance would grow with time gradually leading to instability; our goal is then to find the eigenvalue with the largest real part (the most unstable mode).

By searching for the zero of the largest eigenvalue ($s_r = 0$), we construct a neutral curve for asymptotic stability of the basic flow; the zeros are located by varying La^{-1} while holding l fixed. The resulting marginal stability curve displayed in the La^{-1}, l plane is shown in Figure 1. The area on the top left are regions where all modes are stable, and the bottom right are the region where at least one mode of instability exist.

Since it was proposed that the Langmuir circulations arise from the instability of the CL-equation, we are interested in the unstable region. To gain a further understanding on the behavior of the growth rate in the unstable region, we plot the distribution of growth rate s_r in Figure 2, where all values of $s_r < 0$ are filtered out. From Figure 2 we can observe that the growth rate has a steep edge on the lower part of the wavenumber spectrum (approximately $l < 10$), and that with the increased La^{-1} the range of unstable wavelength increases. The location of the maximum growth rate is sought for in Figure 3; additionally, the percentage distribution compared with the maximum growth rate on fixed La^{-1} is shown.

If the vertical structures in the numerical simulations by Tsai *et al.* (2015) and the experiments of Savelyev *et al.* (2012) are induced by the CL2 instability mechanism,

the spacing of the vortex pairs should reflect the least unstable wavenumber predicted in our analysis. In Figure 4 we have plotted the numerical simulation and experimental data on our instability diagram, here solid symbols represent spacing computed from numerical simulations by Tsai *et al.* (2015), while open symbols represents experimental measurements by Savelyev *et al.* (2012).

The numerical simulations are results of wavelength $\lambda = 7.5, 12.5, 15, 20$ cm from left to right, the friction velocity associated with (2.43) is $u_* = (2\nu\sigma)^{1/2}ak$ and the corresponding reciprocal Lamgmuir number is

$$La = \frac{\nu}{\sqrt{2}a^2\sigma} = \frac{2\pi^{\frac{3}{2}}\nu}{g^{\frac{1}{2}}(ak)^2\lambda^{\frac{3}{2}}},$$

from which we have La^{-1}, and the nondimensional wavenumber l is estimated from the amount of streaks in the streamwise direction. From Figure 4 we see that the numerical simulation is around 95%~99% of the maximum growth rate; for the shortest wavelength ($\lambda = 7.5$ cm), it almost coincides with the largest wavenumber, for the other cases they remain within the range of 95%~99%. Wavenumbers of predominant spacing of Savelyev *et al.* (2012) are not as concentrated, but all fall within the range of 90% of the maximum growth rate. These are as with the findings in Tsai *et al.* (2017). Comparison of the stability curve using Galerkin method and Chebyshev collocation method is shown in Appendix C.2.

23
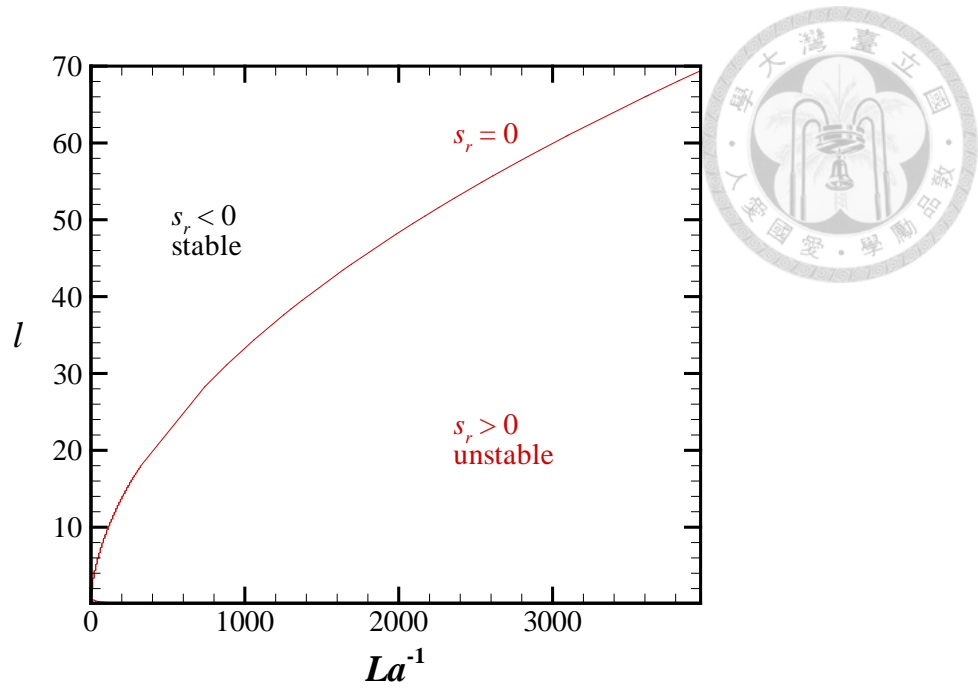
FIGURE 1. Marginal stability curve.

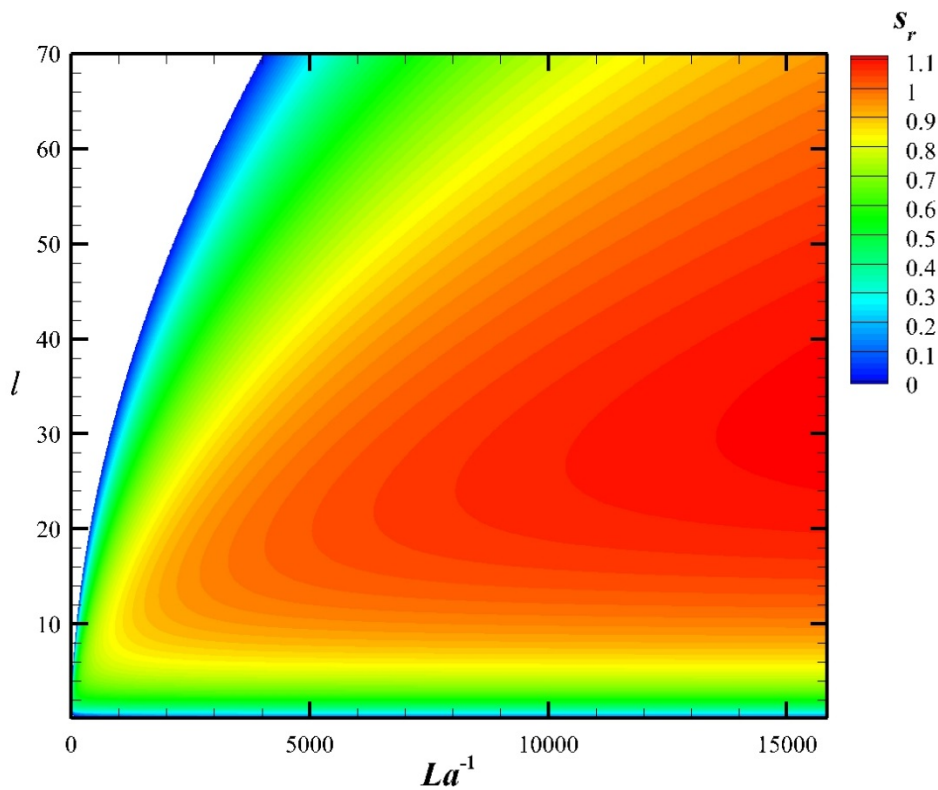FIGURE 2. Instability diagram of the CL-equation, showing the distribution of growth rate s_r for the unstable range of wavenumber l and reciprocal Langmuir number La^{-1}.
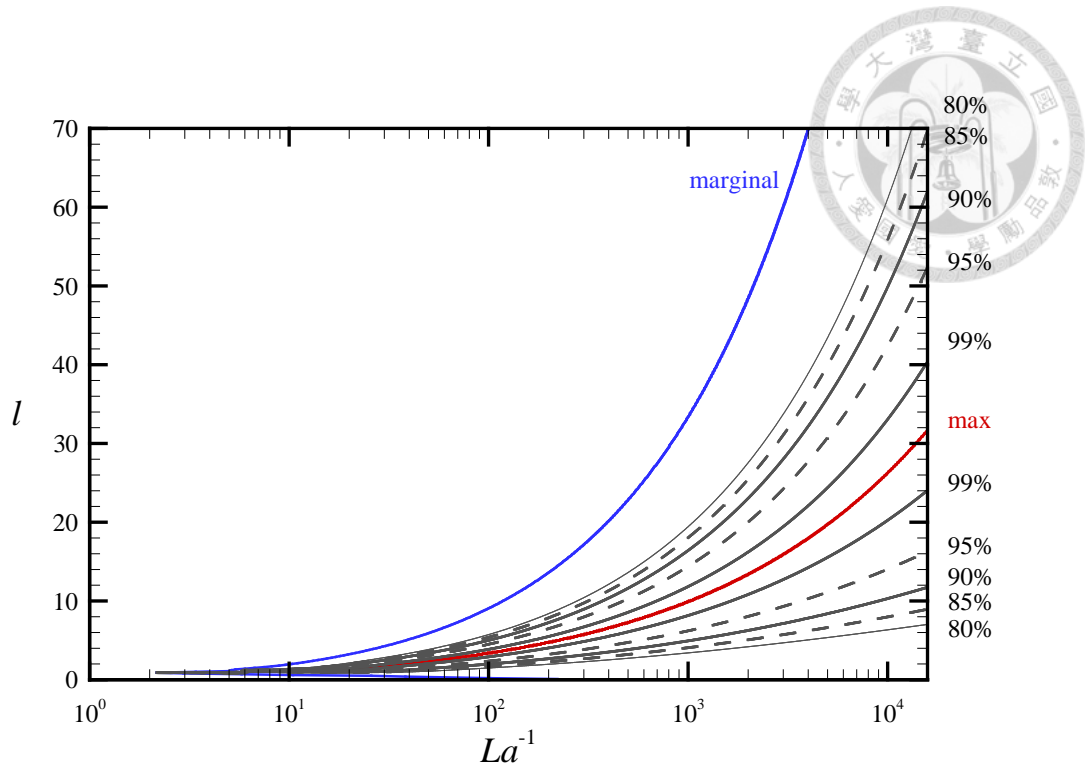
24

FIGURE 3. Stability diagrams of the CL-equation (log scale).
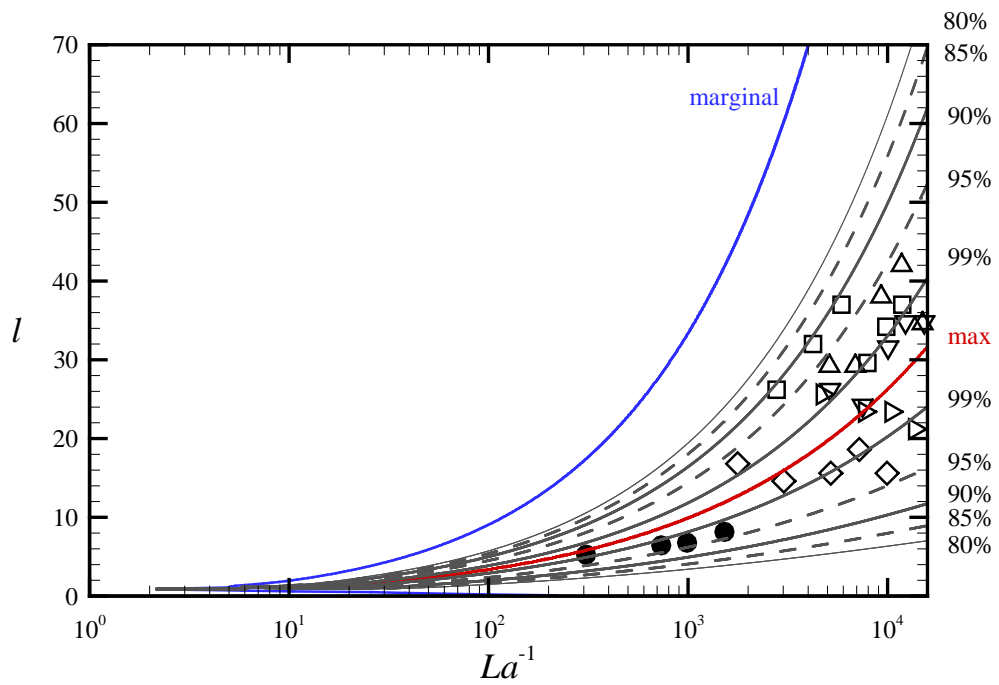

FIGURE 4. Stability diagrams of the CL-equation (log scale) compared with numerical simulation (solid symbols) and experimental results (open symbols).

25

4.2 *Eigenvalue Spectrum in Complex Plane*

Previous stability diagrams only shows the maximum value eigenvalues, interested in the behavior of the whole spectrum, we plot all the eigenvalues within the complex plane. We have selected both stable ($l = 10, La^{-1} = 100$) and unstable ($l = 10, La^{-1} = 1000$) cases.

Eigenvalue spectra for the stable case of $l = 10, La^{-1} = 100$ using $N = 30$ is shown in Figure 5(a). For the stable case, all growth rates are negative, a close up view of the eigenvalues near the least stable mode is shown in Figure 5(b). Since the increased order N would lead to gained amount of eigenvalues, spectrums for $N = 40$ and $N = 50$ are shown in Figure 6 and Figure 7. As the spectrum grows more dense with the increase amount of N, so does the maximum absolute value of s_r, but the maximum (real) value remains fixed.

For the unstable case of $l = 10, La^{-1} = 1000$, the spectrum corresponding to $N = 30, 40, 50$ are shown in Figure 8-10. (For Figure 5-10 the eigenvalues with negative real part are represented by blue squares while ones with positive real part are red dots.) The real part of the spectrum corresponding to different N is shown in Figure 11 for an more straightforward comparison of the effect of increasing N.

Similar to the stable case, the spectrum for the stable modes increase with the amount of N, while the value of the least stable mode remains fixed, the gained amount of eigenvalues increase in the direction beyond this point, suggesting the filling in of a continuous spectrum.

For the unstable modes, it can be seen that more than one unstable mode exists. Furthermore, with increased N the amount of unstable modes remains the same (10 modes) and are of fixed values. Unlike the continuous spectrum observed in the negative s_r plane, the unstable modes are of discrete values, meaning that only specific

26

modes can be observed. Additionally, the eigenvalue with the largest real part (both negative and positive) is always real. From these results, it seems that the unstable configurations are associated with real, discrete spectrum in the positive s_r plane as well as a continuous spectrum in the negative s_r plane, similar to the findings mentioned in Leibovich & Paolucci (1981).

FIGURE 5. (a) Full spectrum of eigenvalues for $l = 10, La^{-1} = 100, N = 30$ in the complex plane. (b) Close-up view of the eigenvalues in the least stable region.

FIGURE 6. (*a*) Full spectrum of eigenvalues for $l = 10, La^{-1} = 100, N = 40$ in the complex plane. (*b*) Close-up view of the eigenvalues in the least stable region.
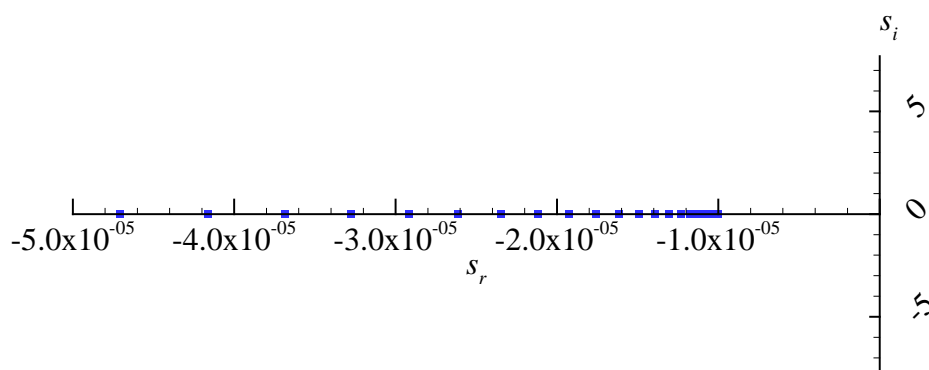
FIGURE 7. (*a*) Full spectrum of eigenvalues for $l = 10, La^{-1} = 100, N = 50$ in the complex plane. (*b*) Close-up view of the eigenvalues in the least stable region.

28
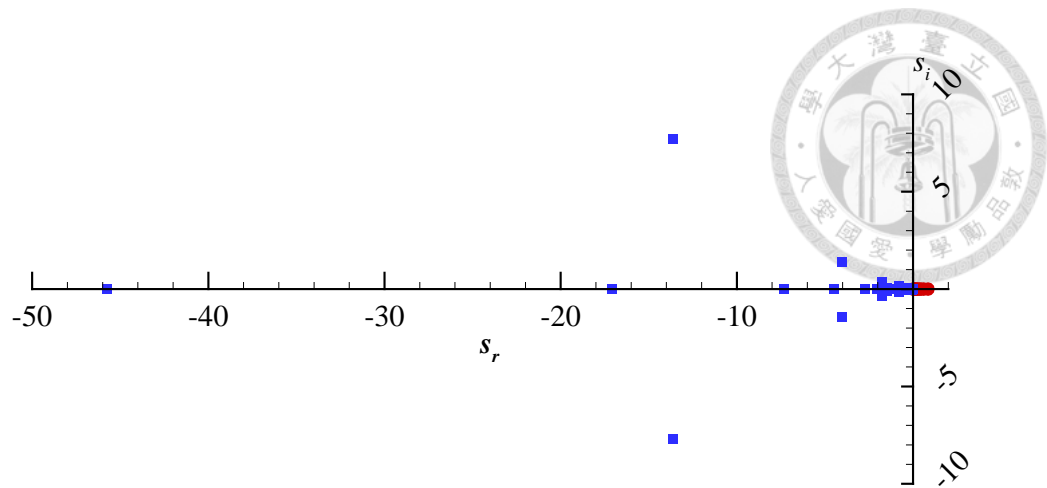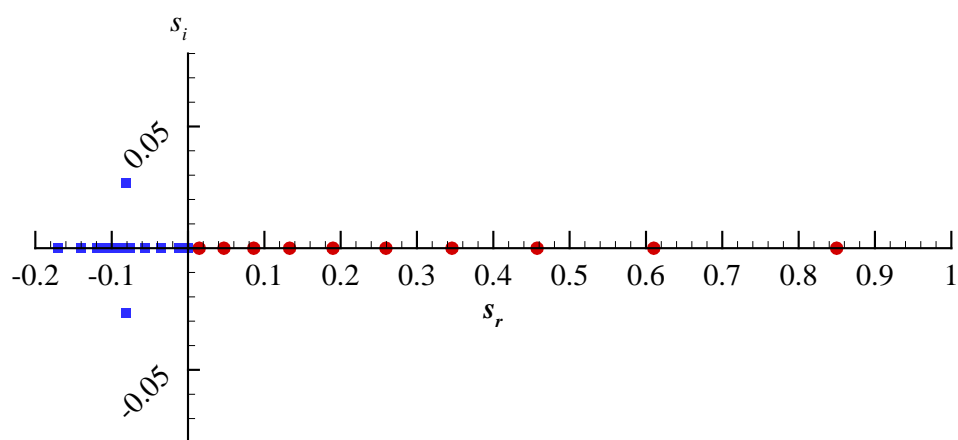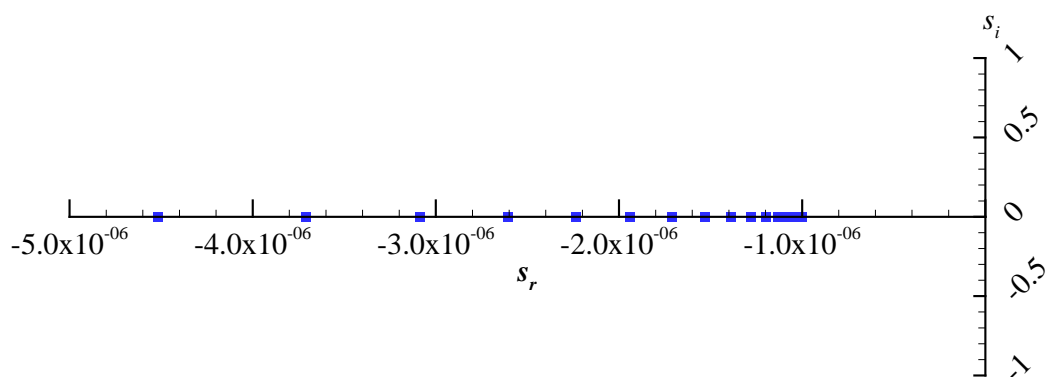
FIGURE 8. (*a*) Full spectrum of eigenvalues for $l = 10, La^{-1} = 1000, N = 30$ in the complex plane. (*b*) Close-up view of the eigenvalues in the positive s_r section. (*c*) Close-up view of the eigenvalues in the least stable region.

29
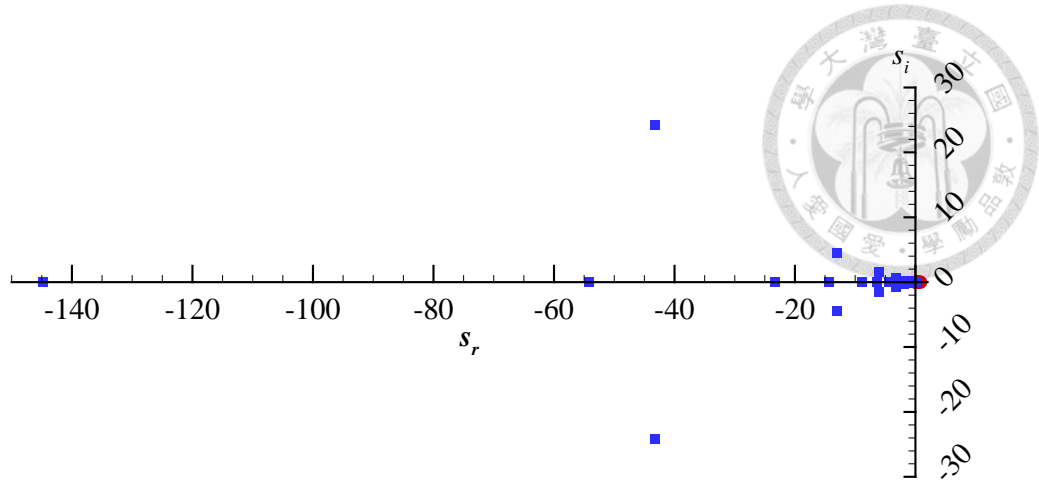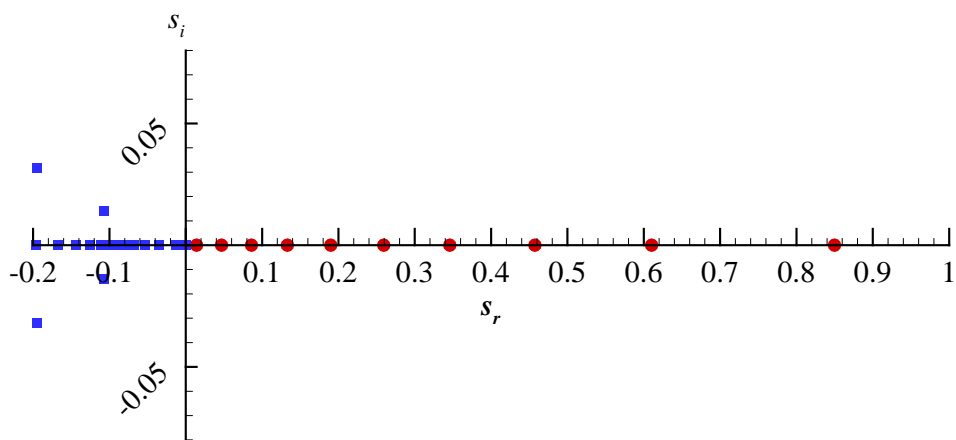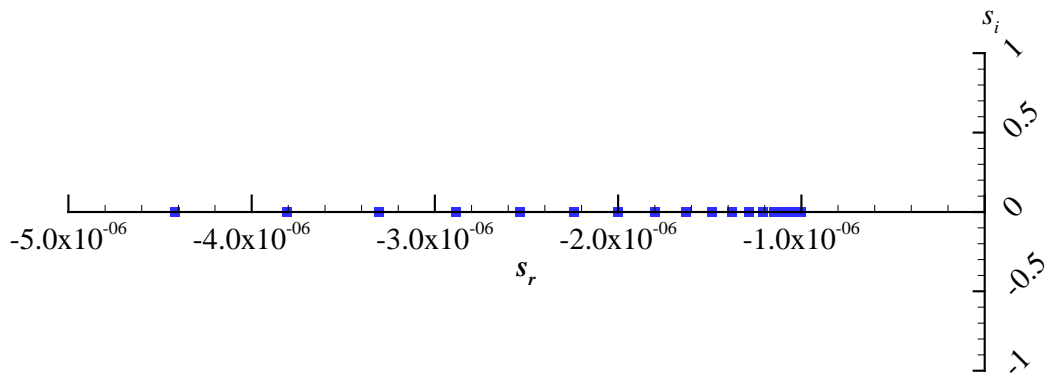
FIGURE 9. (a) Full spectrum of eigenvalues for $l = 10, La^{-1} = 1000, N = 40$ in the complex plane. (b) Close-up view of the eigenvalues in the positive s_r section. (c) Close-up view of the eigenvalues in the least stable region.
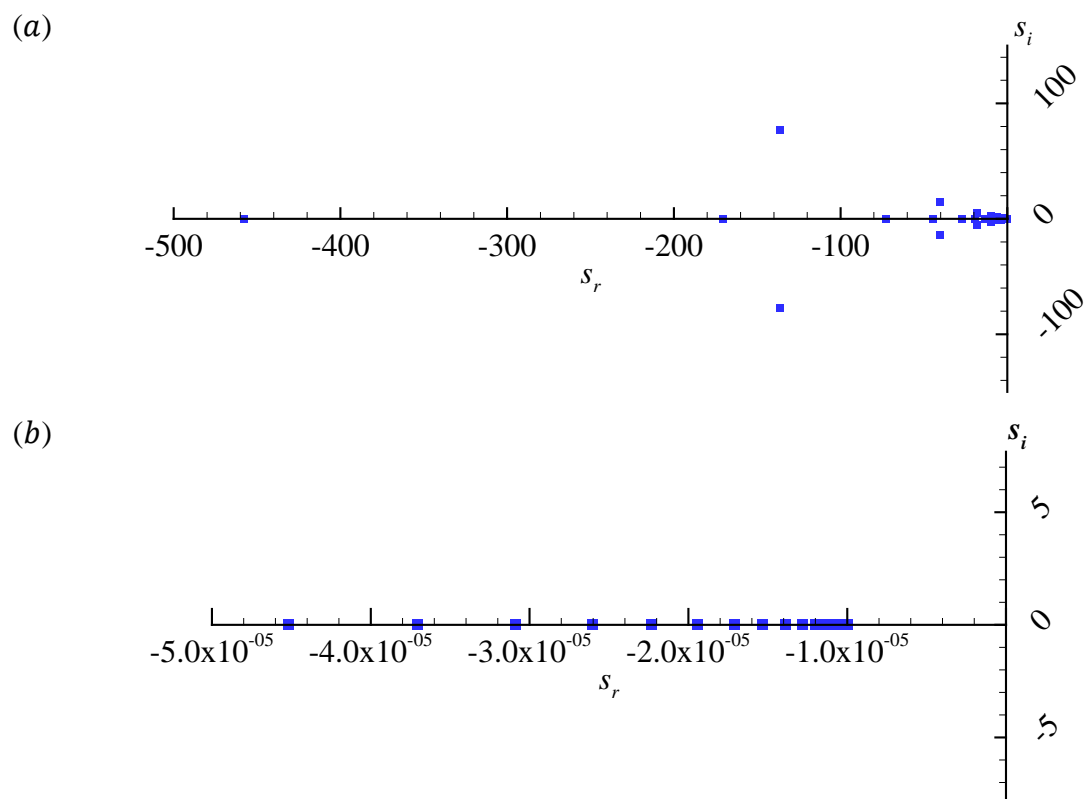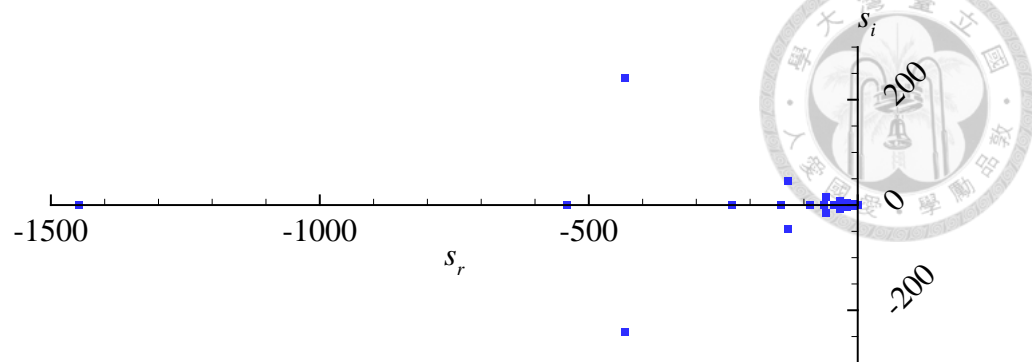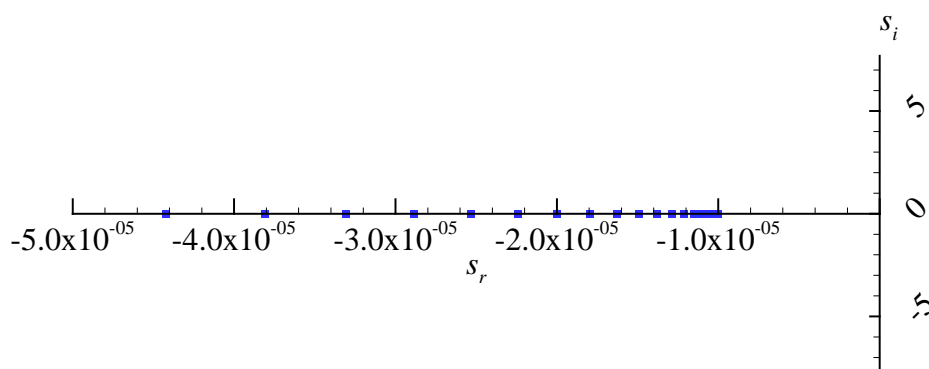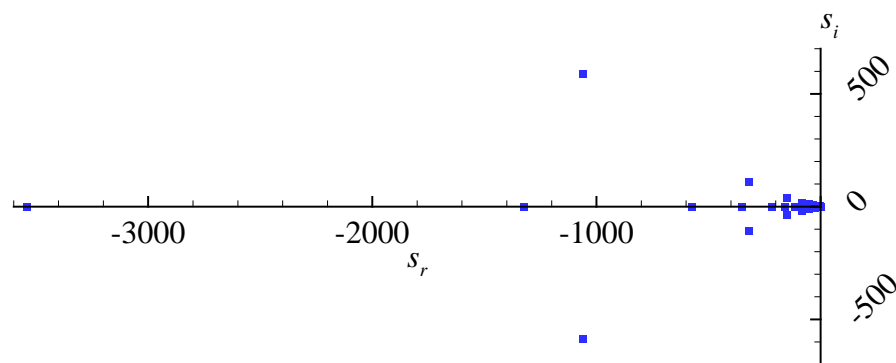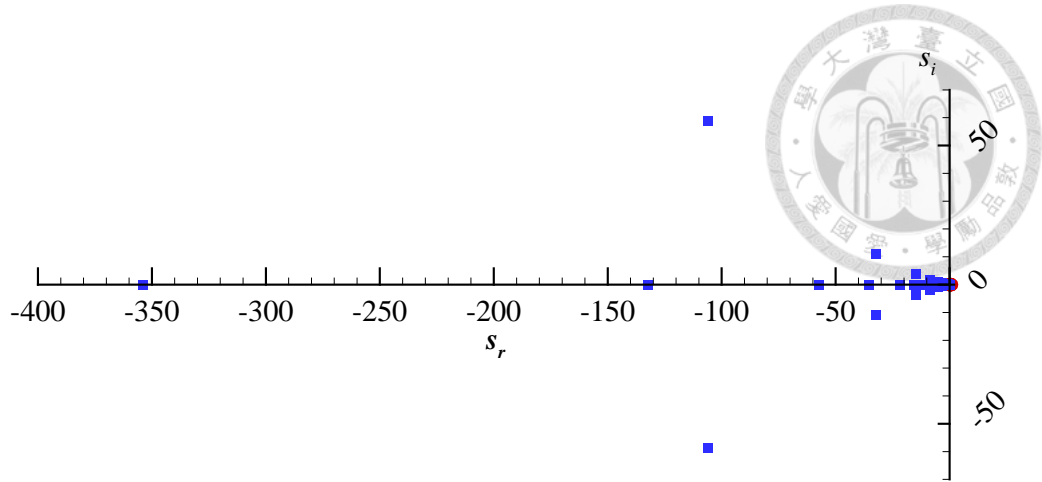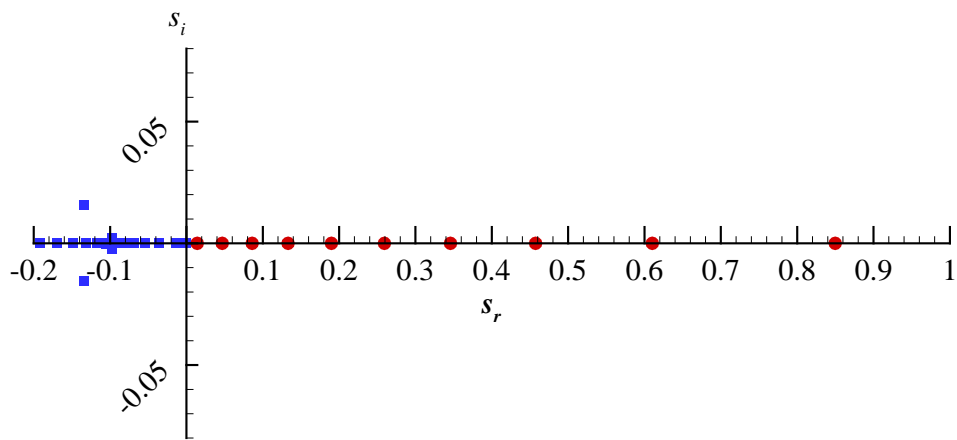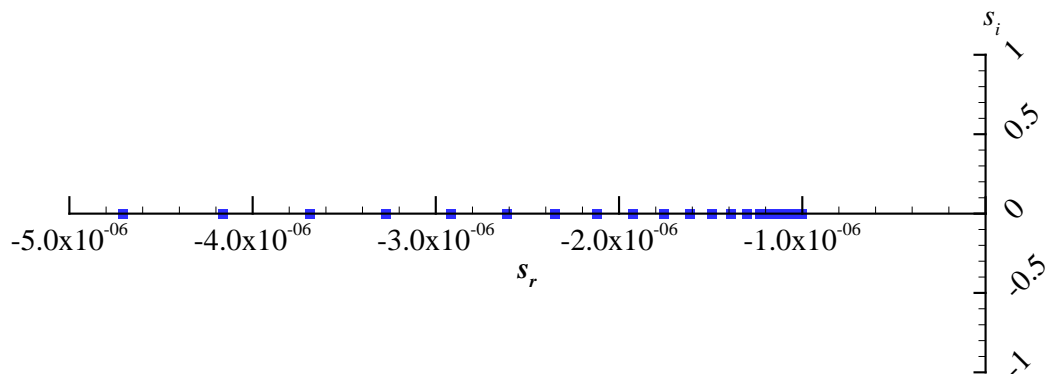
FIGURE 10. (*a*) Full spectrum of eigenvalues for $l = 10, La^{-1} = 1000, N = 50$ in the complex plane. (*b*) Close-up view of the eigenvalues in the positive s_r section. (*c*) Close-up view of the eigenvalues in the least stable region.

31
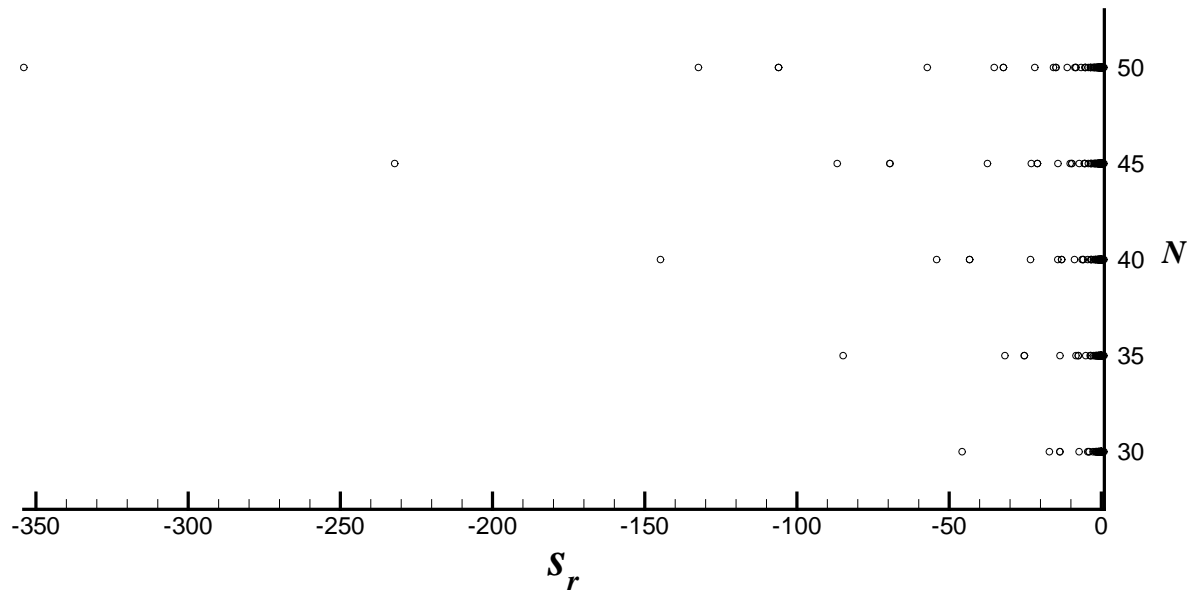
FIGURE 11. The real parts of the spectrum for $l = 10, La^{-1} = 1000$ with various N.

4.3   *Growth Rate of Most Unstable Mode / Second Mode*
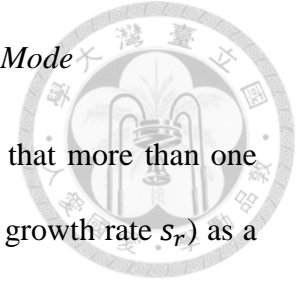
From the eigenvalue results in the previous section, it is clear that more than one unstable mode exist. Plots of the top three most unstable mode (the growth rate s_r) as a function of the wavenumber l while holding fixed reciprocal Langmuir numbers $La^{-1} = 100, 1000, 10000$ are shown in Figure 12-14, note that the values within the range $l < 1$ might not be accurate, as mentioned in section 3.3 the results did not converge. We observe that the second and third unstable modes have similar behavior with the most unstable mode, and with higher reciprocal Langmuir number, the range of unstable wavenumber increases, as well as the maximum growth rate. The growth rate of collocation method and Galerkin method is briefly compared in Appendix C.3.
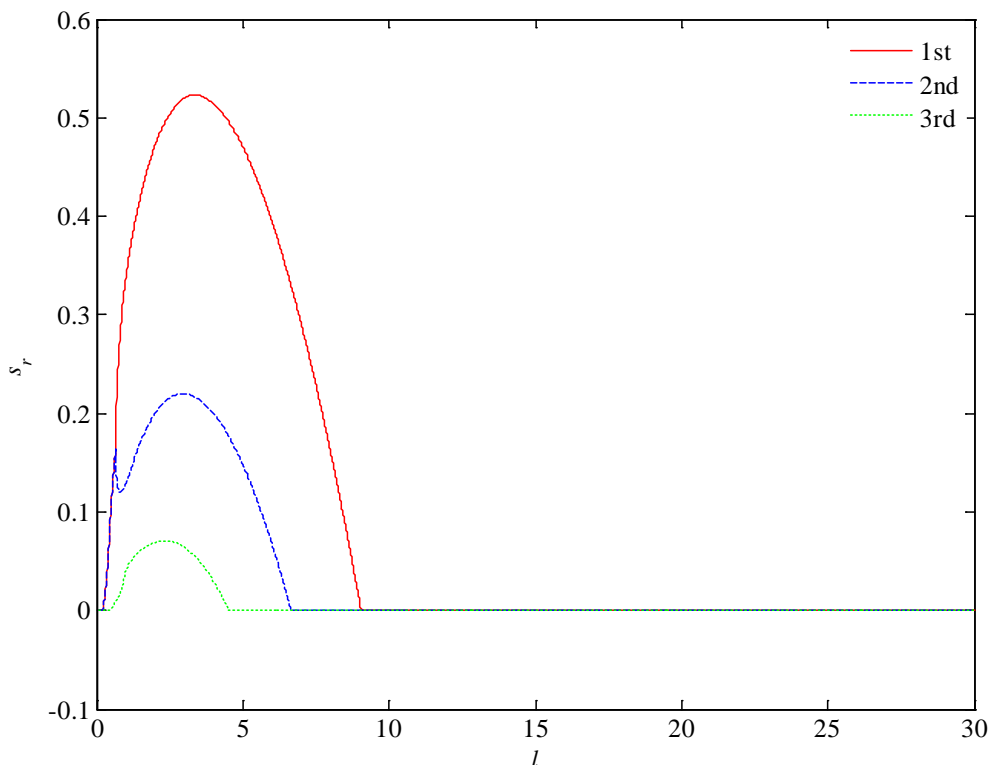
FIGURE 12. The growth rate of the first mode (solid line), second mode (dashed line), and third mode (dotted line) as a function of the wavenumber l for $La^{-1} = 100$.

33
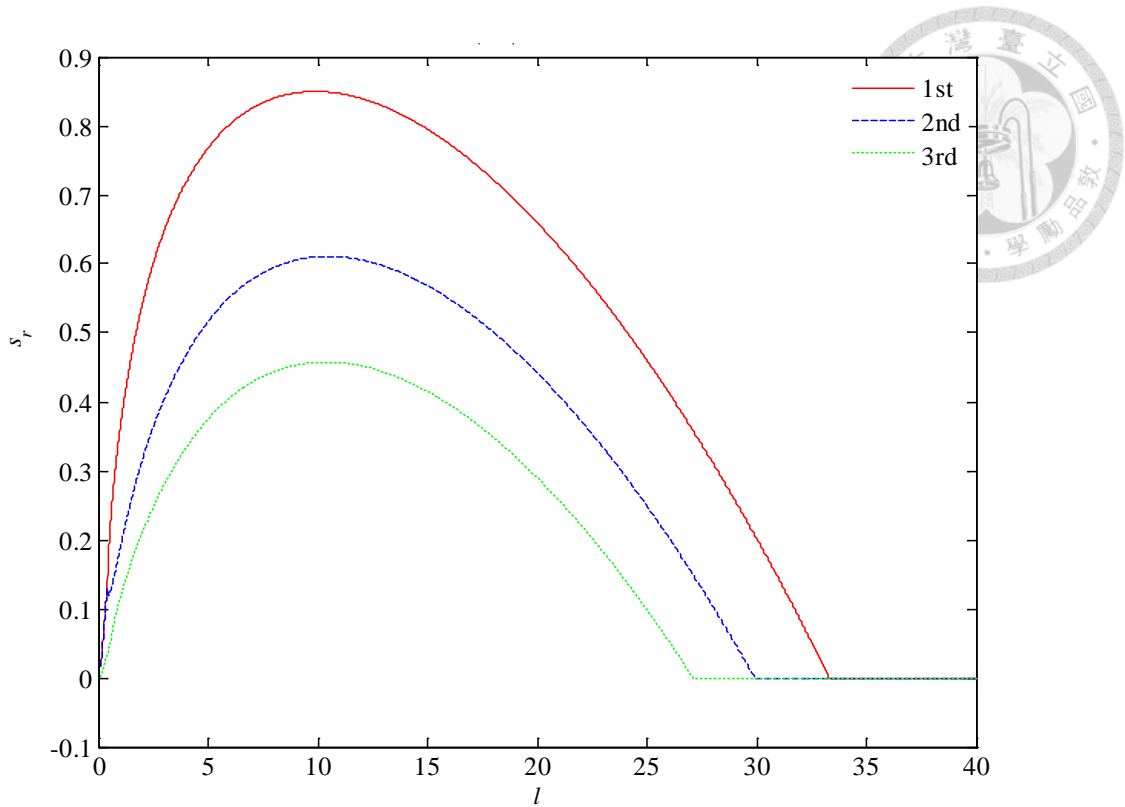
FIGURE 13. The growth rate of the first mode (solid line), second mode (dashed line), and third mode (dotted line) as a function of the wavenumber l for $La^{-1} = 1000$.
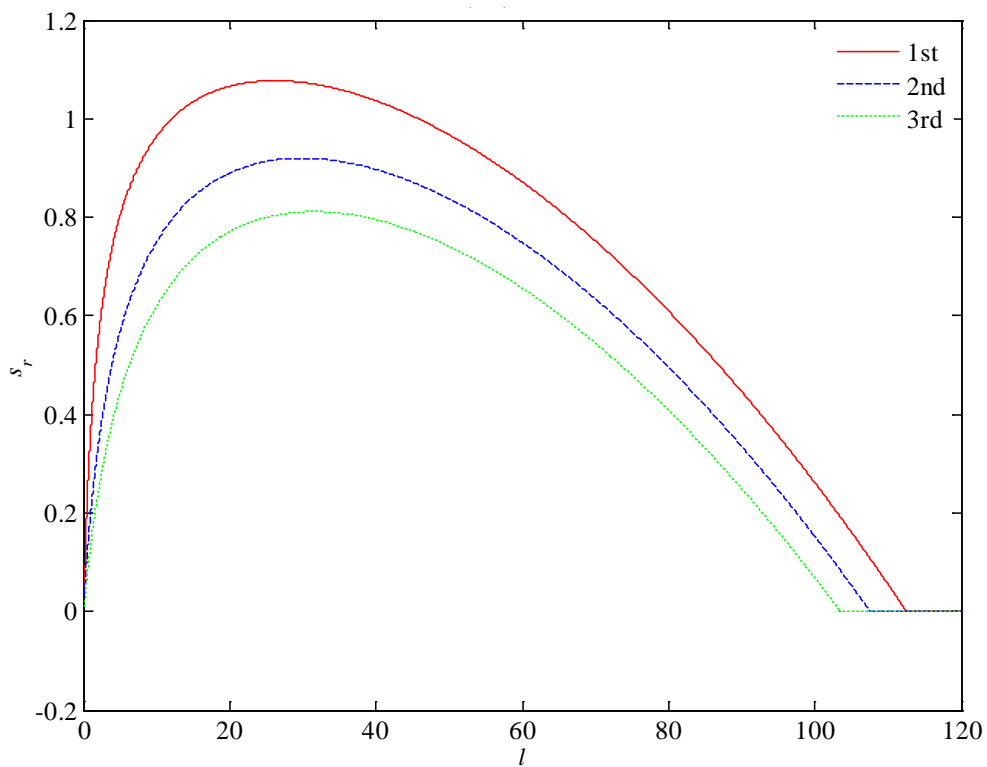
FIGURE 14. The growth rate of the first mode (solid line), second mode (dashed line), and third mode (dotted line) as a function of the wavenumber l for $La^{-1} = 10000$.

34
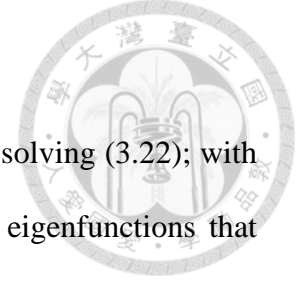
The velocity of the most unstable mode can be calculated after solving (3.22); with the eigenvalue of the most unstable mode and the corresponding eigenfunctions that contain the coefficients of $\hat{u}(z_c)$ and $\hat{w}(z_c)$ of the expansion (3.12), we can calculate the velocities from (3.2) as

$$u(y, z_c, t) = \text{Re}\{\hat{u}(z_c)e^{ily+st}\},\tag{4.1}$$

$$v(y, z_c, t) = \text{Re}\left\{-\frac{1}{il}\frac{\partial \hat{w}(z_c)}{\partial z}e^{ily+st}\right\},\tag{4.2}$$

$$w(y, z_c, t) = \text{Re}\{\hat{w}(z_c)e^{ily+st}\}.\tag{4.3}$$

The spanwise velocity v cannot be solved directly since we had previously replace it with the vertical velocity w using the continuity equation, this relation is now used again to retrieve the spanwise velocity in (4.2).

Since the numerical simulations of Tsai *et al.* (2015) lies roughly around $La^{-1} = 1000$, we look into the velocity profile corresponding to the most unstable mode which is the case $l = 10, La^{-1} = 1000$; the velocity profile is as in Figure 15, plotted for the range $0 \sim 2\pi$ in the spanwise direction y with a uniform spacing of 500 points. In Figure 15 where $l = 10$, the spanwise disturbance wavelength is a tenth of (streamwise) surface wave length, and we can observe 10 pairs of counter-rotating vortices.

The vortices lay within a thin layer near the surface; the close up view of the streamwise velocity profile is shown in Figure 16, as well as the streamlines of spanwise velocity v and vertical velocity w. We have scaled (normalized) the velocities by the largest component out of u, v, w, which in this case is the streamwise velocity u.

Since the velocities are averaged values, they do not represent the actual velocity field but shows the main trend. The apparent feature of counter-rotating vortices

indicates the formation of the convergent and divergent zones near the surface, which could in turn generate streaks along the surface. The streamwise velocity magnitude near the surface is greater than the section below, indicating stronger action at the surface.
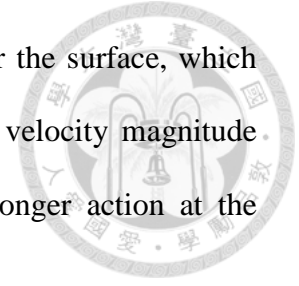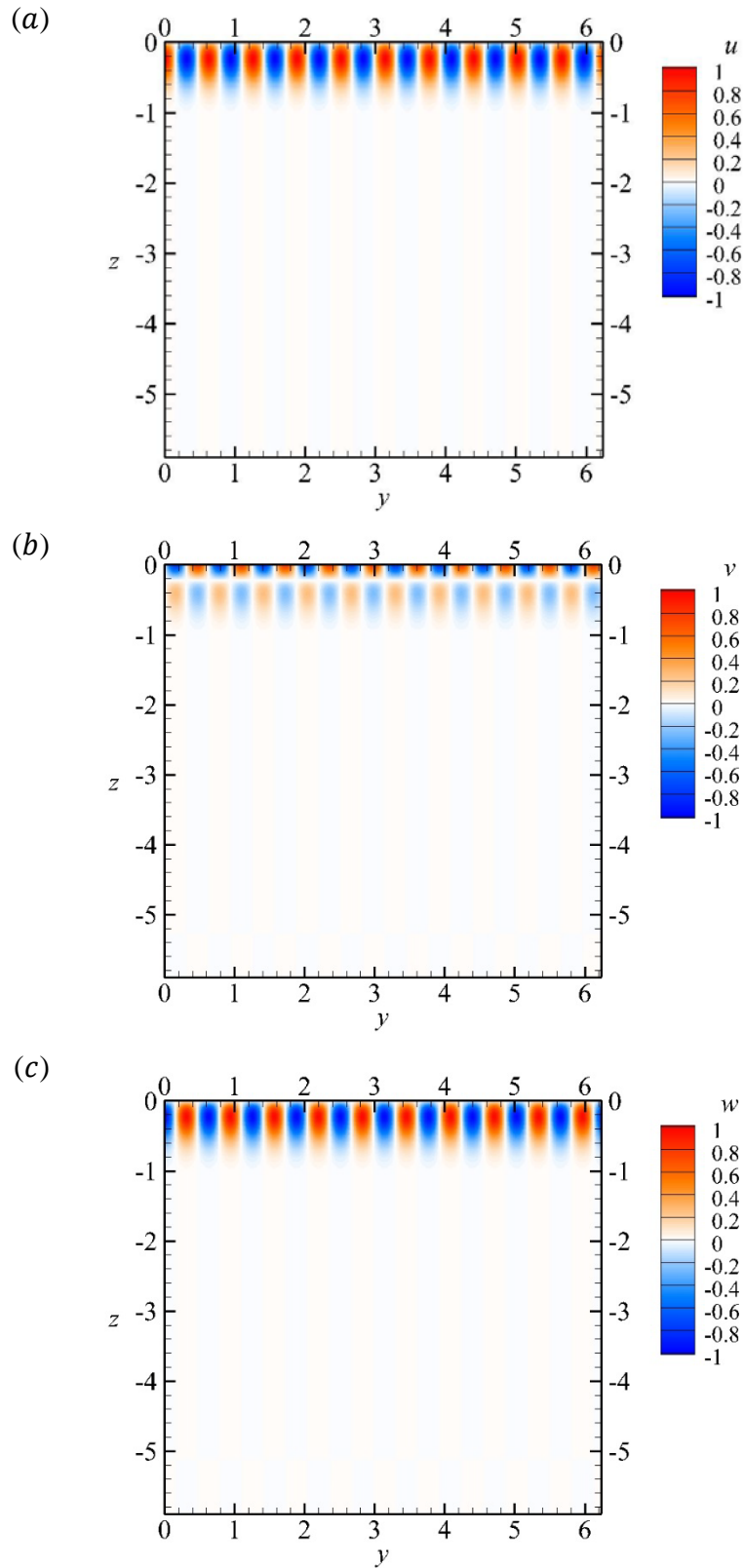
FIGURE 15. Normalized velocity profile of (a) streamwise, (b) spanwise, and (c) vertical velocity for the most unstable mode at $l = 10, La^{-1} = 1000$.
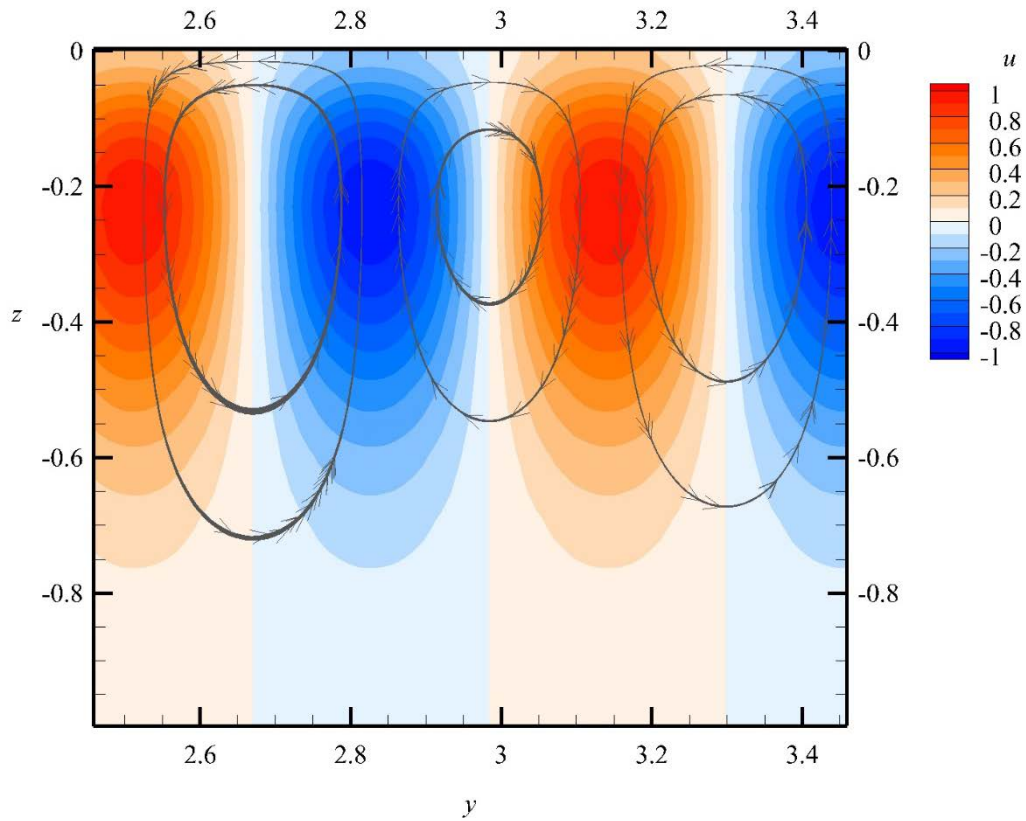
FIGURE 16. Close-up view of the streamwise velocity u with streamlines of spanwise velocity v and vertical velocity w for the most unstable mode at $l = 10, La^{-1} = 1000$.

Chapter 5.   Conclusion

The CL-equations are nonlinear equations governing the Langmuir circulations, which are thought to be formed from the interactions between the Lagrangian drift of the surface waves u_s and the mean shear current U driven by the wind. The equation can be adapted to the flow of free-propagating (non-breaking) surface waves, by replacing the wind stress by the shear stress τ from the viscous effects of the waves. Linear instability of the CL-equations is studied by implementing the Chebyshev collocation method; the system of ordinary differential equation that resulted from introducing normal mode expansions to the partial differential equations are solved. We had checked the validity of this method on comparing with the Orr-Sommerfeld stability solved by Orszag (1971).

The spanwise wavelength of the most unstable mode is close to the spacing of counter-rotating vortices observed in numerical simulations by Tsai *et al.* (2015) and laboratory experiments of Savelyev *et al.* (2012); furthermore, the resulting velocity profiles of the most unstable mode also display an array of counter-rotating vortex pairs. Thus, it is highly probable that the streamwise vortices under the free-propagating surface wave are excited by the CL2 instability. Additionally, during an unstable case, more than one unstable mode exists, and the eigenvalue spectrum appears to comprised of a discrete spectrum for positive s_r (if unstable), and a continuous spectrum for negative s_r, similar to the findings mentioned in Leibovich & Paolucci (1981).

Our results from using Chebyshev collocation method is in agreement with Tsai *et al.* (2017), where they used the Galerkin method. On understanding the methodology, we can apply the Chebyshev collocation method for other types of stability analysis for future work.

References
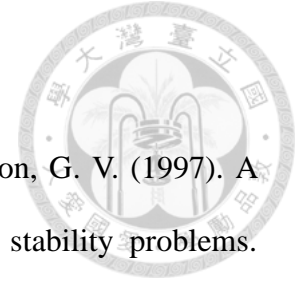
Boomkamp, P. A. M., Boersma, B. J., Miesen, R. H. M., & Beijnon, G. V. (1997). A Chebyshev collocation method for solving two-phase flow stability problems. *Journal of Computational Physics*, *132*(2), 191-200.

Craik, A. D. D. (1982). The drift velocity of water waves. *Journal of Fluid Mechanics*, *116*, 187-205.

Craik, A. D., & Leibovich, S. (1976). A rational model for Langmuir circulations. *Journal of Fluid Mechanics*, *73*(3), 401-426.

Drazin, P. G., & Reid, W. H. (1981). *Hydrodynamic Stability*. Cambridge university press.

Langmuir, I. (1938). Surface motion of water induced by wind. *Science*, *87*(2250), 119-123.

Leibovich, S. (1977*a*). On the evolution of the system of wind drift currents and Langmuir circulations in the ocean. Part 1. Theory and averaged current. *Journal of Fluid Mechanics*, *79*(4), 715-743.

Leibovich, S. (1977*b*). Convective instability of stably stratified water in the ocean. *Journal of Fluid Mechanics*, *82*(3), 561-581.

Leibovich, S. (1983). The form and dynamics of Langmuir circulations. *Annual Review of Fluid Mechanics, 15*(1), 391-427.

Leibovich, S., & Paolucci, S. (1981). The instability of the ocean to Langmuir circulations. *Journal of Fluid Mechanics*, *102*, 141-167.

Lele, S. K. (1985). Some problems of hydrodynamic stability arising in geophysical fluid dynamics.

Longuet-Higgins, M. S. (1953). Mass transport in water waves. *Philosophical Transactions of the Royal Society of London A: Mathematical, Physical and Engineering Sciences*, *245*(903), 535-581.

Orszag, S. A. (1971). Accurate solution of the Orr–Sommerfeld stability equation. *Journal of Fluid Mechanics*, *50*(4), 689-703.

Phillips, W. R. C. (2001). On an instability to Langmuir circulations and the role of Prandtl and Richardson numbers. *Journal of Fluid Mechanics*, *442*, 335-358.

Phillips, W. R. C., & Dai, A. (2014). On Langmuir circulation in shallow waters. *Journal of Fluid Mechanics*, *743*, 141-169.

Savelyev, I. B., Maxeiner, E., & Chalikov, D. (2012). Turbulence production by nonbreaking waves: Laboratory and numerical simulations. *Journal of Geophysical Research: Oceans*, *117*(C11).

Tsai, W. T., Chen, S. M., & Lu, G. H. (2015). Numerical evidence of turbulence generated by nonbreaking surface waves. *Journal of Physical Oceanography*, *45*(1), 174-180.

Tsai, W. T., Lu, G. H., Chen, J. R., Dai, A., & Phillips, W. R. (2017). On the Formation of Coherent Vortices beneath Nonbreaking Free-Propagating Surface Waves. *Journal of Physical Oceanography*, *47*(3), 533-543.

Appendix A.   Viscous Stability Analysis – Plane Poiseuille Flow

Here we present the steps to solve the Orr-Sommerfeld equation (of the plane Poiseuille flow) numerically using Chebyshev polynomials expansions and point collocation, the resulting generalized eigenvalue problem is solved using QZ-algorithm. For the plane Poiseuille flow, the critical Reynolds number is found to be approximately 5772.

A.1   *Problem Formulation*

We wish to study the plane Poiseuille flow in a channel. Setting the streamwise direction as the $\tilde{x}$-coordinate (unit vector $\boldsymbol{i}$), spanwise direction $\tilde{y}$-coordinate (unit vector $\boldsymbol{j}$), and let $\tilde{z}$ positive vertically upwards (unit vector $\boldsymbol{k}$). The flow is bounded by the two plans $\tilde{z} = \tilde{z}_1$ and $\tilde{z}_2$, both are rigid boundaries where the no slip condition holds. The dimensional Navier-Stokes equation and the continuity equation are

$$\rho \left(\frac{\partial \widetilde{\boldsymbol{v}}}{\partial t} + \widetilde{\boldsymbol{v}} \cdot \widetilde{\boldsymbol{\nabla}} \widetilde{\boldsymbol{v}} \right) = -\widetilde{\boldsymbol{\nabla}} p + \mu \widetilde{\boldsymbol{\nabla}}^2 \widetilde{\boldsymbol{v}}, \tag{A 1}$$

$$\widetilde{\boldsymbol{\nabla}} \cdot \widetilde{\boldsymbol{v}} = 0, \tag{A 2}$$

here the superscript "wiggle" denotes dimensional terms, while the bold symbol marks vector quantities. We measure all lengths in units of the channel half-width and velocities in units of the maximum velocity of the undisturbed stream velocity $\widetilde{\boldsymbol{U}} = \widetilde{U}(\tilde{z})\boldsymbol{i}$. Hence the characteristic velocity and length scales are

$$[\mathcal{V}] = max\big|\widetilde{U}(\tilde{z})\big|, \qquad [\mathcal{L}] = \frac{1}{2}(\tilde{z}_2 - \tilde{z}_1). \tag{A 3}$$

Set dimensionless parameters according to the characteristic scales as

$$t = \frac{\tilde{t}[\mathcal{V}]}{[\mathcal{L}]}, \qquad \boldsymbol{x} = \frac{\widetilde{\boldsymbol{x}}}{[\mathcal{L}]}, \qquad \boldsymbol{v} = \frac{\widetilde{\boldsymbol{v}}}{[\mathcal{V}]},$$

$$p = \frac{\tilde{p}}{\rho[\mathcal{V}]^2}, \qquad \boldsymbol{U} = \frac{\widetilde{\boldsymbol{U}}}{[\mathcal{V}]} \equiv U(z)\boldsymbol{i}, \tag{A 4}$$

42

introduce (A 4) into (A 1) and (A 2) to get the non-dimensional governing equations

$$\frac{\partial \boldsymbol{v}}{\partial t} + \boldsymbol{v} \cdot \nabla \boldsymbol{v} = -\nabla p + \frac{1}{Re} \nabla^2 \boldsymbol{v}, \tag{A 5}$$

$$\nabla \cdot \boldsymbol{v} = 0, \tag{A 6}$$

where $Re = \frac{\rho [\mathcal{V}][\mathcal{L}]}{\mu}$ is the Reynolds number, and the no slip boundary conditions are

$$\boldsymbol{v} = 0 \quad \text{at} \quad z = \pm 1. \tag{A 7}$$

For the plane Poiseuille flow, the basic steady flow satisfies the governing equations and both of the boundary condition, leading to the (dimensionless) form,

$$(z) = 1 - z^2, \qquad \frac{dP}{dx} = \text{constant} \ (-1 \le z \le 1). \tag{A 8}$$

To study the stability of this flow, we add disturbance to the basic flow by setting

$$\boldsymbol{u}(\boldsymbol{x}, t) = U(z)\boldsymbol{i} + \boldsymbol{u}'(\boldsymbol{x}, t), \tag{A 9}$$

$$p(\boldsymbol{x}, t) = \bar{P}(x) + p'(\boldsymbol{x}, t), \tag{A 10}$$

where $\boldsymbol{u}'$ is the disturbance velocity and p' is the disturbance pressure. Substituting these expressions into (A 5)-(A 6) and neglecting the quadratic terms of the disturbance velocity, we obtain the linearized governing equations

$$\frac{\partial u'}{\partial t} + U \frac{\partial u'}{\partial x} + w' \frac{dU}{dz} = -\frac{\partial p'}{\partial x} + \frac{1}{Re} \nabla^2 u', \tag{A 11}$$

$$\frac{\partial v'}{\partial t} + U \frac{\partial v'}{\partial x} = -\frac{\partial p'}{\partial y} + \frac{1}{Re} \nabla^2 v', \tag{A 12}$$

$$\frac{\partial w'}{\partial t} + U \frac{\partial w'}{\partial x} = -\frac{\partial p'}{\partial z} + \frac{1}{Re} \nabla^2 w', \tag{A 13}$$

$$\nabla \cdot \boldsymbol{v}' = 0. \tag{A 14}$$

A.2 *Normal Mode Expansion*

Since the coefficients in the linearized governing equations only depend on z, the equations admit solutions that depend on x, y, and t exponentially. According, we assume normal modes of the form

$$\boldsymbol{v}'(\boldsymbol{x}, t) = \hat{\boldsymbol{v}}(z) e^{i(kx + my - kct)}, \tag{A 15}$$

$$p'^{(x,t)} = \hat{p}(z) e^{i(kx + my - kct)}, \tag{A 16}$$

it is understood that the physical quantities are obtained by taking the real part of these expressions. Since the flow is unbounded in the x and y direction, the wavenumber components k and m must be real, so that the solutions remain bounded as $x, y \to \pm\infty$. The wave speed c may be complex, i.e. $c = c_r + ic_i$. The expression then represents waves traveling obliquely to the basic flow in the direction $(k, m, 0)$ with the phase speed $kc_r / \sqrt{(k^2 + m^2)}$, and has a varying magnitude in time as $\exp(kc_i t)$. Such wave is stable if $kc_i < 0$, unstable if $kc_i > 0$, and neutrally stable if $kc_i = 0$.

On substitution of the normal modes, the perturbation equations becomes the ordinary differential equations

$$\left(D^2 - (k^2 + m^2) - ikRe(U - c)\right)\hat{u} = Re\frac{dU}{dz}\hat{w} + ikRe\hat{p}, \tag{A 17}$$

$$\left(D^2 - (k^2 + m^2) - ikRe(U - c)\right)\hat{v} = imRe\hat{p}, \tag{A 18}$$

$$\left(D^2 - (k^2 + m^2) - ikRe(U - c)\right)\hat{w} = Re\frac{d\hat{p}}{dz}, \tag{A 19}$$

$$i(k\hat{u} + m\hat{v}) + \frac{d\hat{w}}{dz} = 0, \tag{A 20}$$

where $D = d/dz$. These are the normal mode equations for the three-dimensional disturbances; however, in seeking the sufficient criteria for instability, Squire's theorem shows that in obtaining the minimum critical Reynolds number, it is sufficient to consider only two-dimensional disturbances (Drazin & Reid 1981). Hence considering

44

the two-dimensional case, which is the three-dimensional equation with $m = \hat{v} = 0$, the equations are

$$\left(D^2 - k^2 - ikRe(U - c)\right)\hat{u} = Re\frac{dU}{dz}\hat{w} + ikRe\hat{p}, \qquad (A\,21)$$

$$\left(D^2 - k^2 - ikRe(U - c)\right)\hat{w} = Re\frac{d\hat{p}}{dz}, \qquad (A\,22)$$

$$ik\hat{u} + \frac{d\hat{w}}{dz} = 0. \qquad (A\,23)$$

45
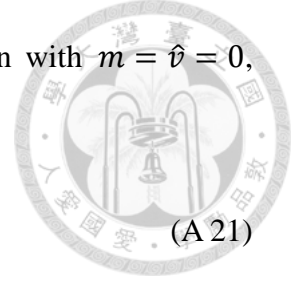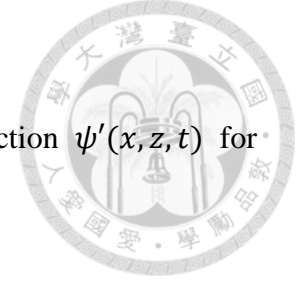
The two-dimensionality allows the definition of a stream function $\psi'(x, z, t)$ for the perturbed field

$$u' = \frac{\partial \psi'}{\partial z}, \qquad w' = -\frac{\partial \psi'}{\partial x}. \tag{A 24}$$

Likewise, we assume normal modes of the form:

$$[u', w', \psi'] = \left[\hat{u}(z), \hat{w}(z), \hat{\phi}(z)\right] e^{ik(x-ct)}, \tag{A 25}$$

then we must have

$$\hat{u}(z) = \frac{d\hat{\phi}(z)}{dz}, \qquad \hat{w}(z) = -ik\hat{\phi}(z). \tag{A 26}$$

Substituting into (A 21)-(A 23), the number of unknowns reduces from 3 to 2:

$$\left(D^2 - k^2 - ikRe(U - c)\right)\frac{\partial \hat{\phi}(z)}{\partial z} = Re\frac{dU}{dz}\left(-ik\hat{\phi}(z)\right) + ikRe\hat{p}, \tag{A 27}$$

$$\left(D^2 - k^2 - ikRe(U - c)\right)\left(-ik\hat{\phi}(z)\right) = Re\frac{d\hat{p}}{dz}, \tag{A 28}$$

the pressure term can be eliminated, reducing to a single equation:

$$(U - c)(D^2 - k^2)\hat{\phi} - U''\hat{\phi} = \frac{1}{ikRe}\left(D^4\hat{\phi} - 2k^2D^2\hat{\phi} + k^2\hat{\phi}\right), \tag{A 29}$$

which is the known Orr-Sommerfeld equation. The boundary conditions at the walls, i.e. the no-slip conditions, requires

$$\hat{\phi} = \frac{d\hat{\phi}}{dz} = 0 \quad \text{at} \quad z = \pm 1. \tag{A 30}$$

We then need to solve the forth-order ordinary differential equation.

A.4 *Chebyshev Collocation Method*

Rearrange the Orr-Sommerfeld equation as

$$\frac{1}{Re}(D^2 - k^2)(D^2 - k^2)\hat{\phi} - ikU(D^2 - k^2)\hat{\phi} + ikU''\hat{\phi} = -ikc(D^2 - k^2)\hat{\phi},$$

since our aim is to find the growth rate kc_i, for simplicity we set $s \equiv -ikc$, hence the term $e^{ik(x-ct)}$ in (A 25) becomes e^{ikx+st}. Furthermore, to avoid dealing with the fourth-order differential term, we introduce

$$\hat{Y} \equiv (D^2 - k^2)\hat{\phi}, \tag{A 31}$$

consequently, our equation reduces to the second-order differential equations

$$\frac{1}{Re}(D^2 - k^2)\hat{Y} - ikU\hat{Y} + ikU''\hat{\phi} = s\hat{Y}, \tag{A 32}$$

$$(D^2 - k^2)\hat{\phi} - \hat{Y} = 0, \tag{A 33}$$

though the number of unknowns has increased, we have dropped the order by two.

To solve the equations numerically, we approximate the eigenfunctions by the truncated Chebyshev expansions

$$\hat{\phi}(z) = \sum_{n=0}^{N} a_n T_n(z), \qquad \hat{Y}(z) = \sum_{n=0}^{N} b_n T_n(z), \tag{A 34}$$

where a_n and b_n are coefficients, and $T_n(z)$ is the n th-degree Chebyshev polynomial of the first kind, defined by $T_n(\cos\theta) = \cos n\theta$, for all non-negative integers n; and N is order of the polynomial. Substitute (A 34) into (A 32)-(A 33) to get

$$ikU'' \sum_{n=0}^{N} a_n T_n(z) + \left(\frac{1}{Re}(D^2 - k^2) - ikU\right) \sum_{n=0}^{N} b_n T_n(z) = s \sum_{n=0}^{N} b_n T_n(z), \tag{A 35}$$

$$\left(\sum_{n=0}^{N} a_n T_n''^{(z)} - k^2 \sum_{n=0}^{N} a_n T_n(z)\right) - \sum_{n=0}^{N} b_n T_n(z) = 0, \tag{A 36}$$

47

here the number of unknowns are now the $2(N+1)$ coefficients of a_n and b_n, therefore the same amount of equations is required to solve for the coefficients. We collocate the approximations at the points

$$z_j = \cos\frac{j\pi}{N}, \qquad j = 1,2,\dots N-1, \tag{A 37}$$

resulting in $2(N-1)$ equations, along with four boundary conditions

$$\phi(-1) = \phi(1) = 0, \qquad \frac{d\phi}{dz}(-1) = \frac{d\phi}{dz}(1) = 0, \tag{A 38}$$

the system of equations can be written as a generalized eigenvalue problem

$$[A]\boldsymbol{a} = s[B]\boldsymbol{a}, \tag{A 39}$$

where $\boldsymbol{a}^{\mathrm{T}} = [a_0, a_1, a_2, \dots a_N, b_0, b_1, b_2, \dots b_N] \in R^{2N+2}$, the detailed elements of matrix $[A]$ and $[B]$ are shown in appendix A.6, we can then solve for the eigenvalue s. The generalized eigenvalue problem is solved using the MATLAB function QZ and eig. The MATLAB code for solving the Orr-Sommerfeld equation had been generously handed out from Dr. Falin Chen.

The eigenvalue solved with different order N under the same parameters ($k = 1, Re = 10000$) as with Orszag (1971) were shown in Table 1. Note that in our computation the eigenvalue we solved for was $s \equiv -ikc$, where in Orszag (1971) the eigenvalue solved is c, therefore had we converted the eigenvalues in Table 1 to c for comparison.

48

A.5 *Marginal Stability Curve*

The marginal stability curve for the plane Poiseuille flow is as shown in Figure 17; the critical Reynolds number found is 5772.31, very close to the value 5772.22 from Orszag (1971).
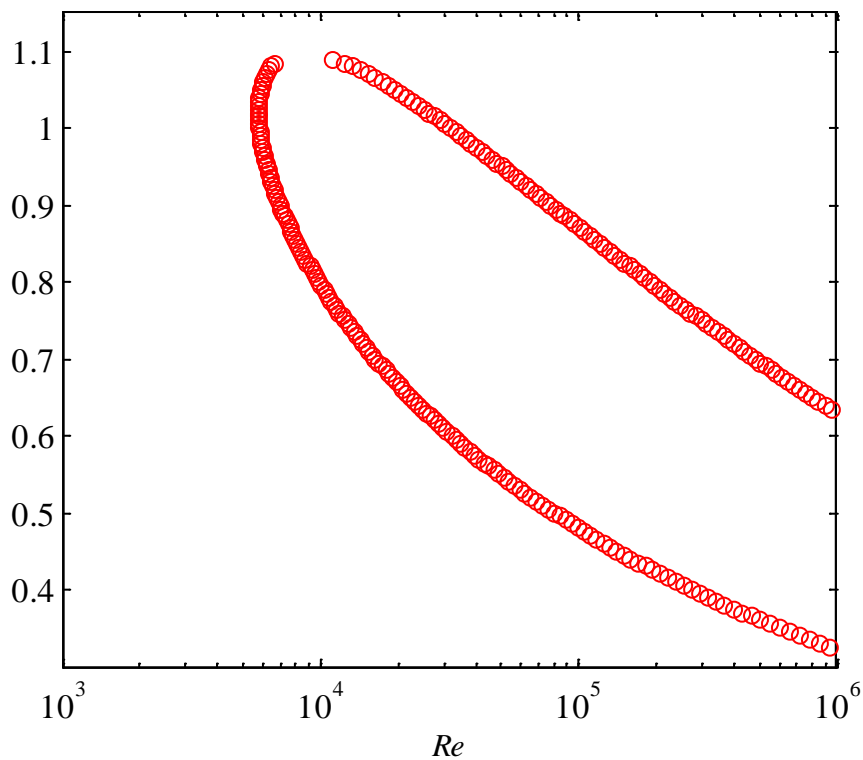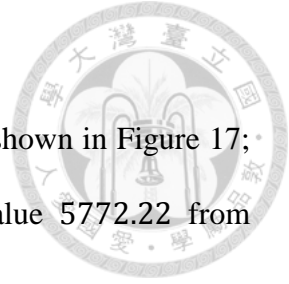
FIGURE 17. Marginal stability curve for the plane Poiseuille flow.

The matrix $[A]$ and $[B]$ from (A 39) are shown here. We have chosen the last four rows to implement the four boundary conditions. Here we have let

$$F_j^n = \left(T_n''(z_j) - k^2 T_n(z_j) \right),$$

while the rest of symbols remains the same as previously defined.

$[A]_{2N+2,2N+2} =$

$$
\begin{bmatrix}
ikU''T_0(z_1) & \dots & ikU''T_N(z_1) & \dfrac{F_1^0}{Re} - ikUT_0(1) & \dots & \dfrac{F_1^N}{Re} - ikUT_N(1) \\[2mm]
\vdots & \ddots & \vdots & \vdots & \ddots & \vdots \\[2mm]
ikU''T_0(z_{N-1}) & \dots & ikU''T_N(z_{N-1}) & \dfrac{F_{N-1}^0}{Re} - ikUT_0(z_{N-1}) & \dots & \dfrac{F_{N-1}^N}{Re} - ikUT_N(z_{N-1}) \\[2mm]
F_1^0 & \dots & F_1^N & -T_0(z_1) & & -T_N(z_1) \\[1mm]
\vdots & \ddots & \vdots & \vdots & \ddots & \vdots \\[1mm]
F_{N-1}^0 & \dots & F_{N-1}^N & -T_0(z_{N-1}) & \dots & -T_N(z_{N-1}) \\[1mm]
T_0(-1) & \dots & T_N(-1) & 0 & \dots & 0 \\[1mm]
T_0(1) & \dots & T_N(1) & 0 & \dots & 0 \\[1mm]
T_0'(-1) & \dots & T_N'(-1) & 0 & \dots & 0 \\[1mm]
T_0'(1) & \dots & T_N'(1) & 0 & \dots & 0
\end{bmatrix}
$$

$[B]_{2N+2,2N+2} =$

$$
\begin{bmatrix}
0 & \dots & 0 & T_0(z_1) & \dots & T_N(z_1) \\
0 & \dots & 0 & T_0(z_2) & \dots & T_N(z_2) \\
\vdots & \ddots & \vdots & \vdots & \ddots & \vdots \\
0 & \dots & 0 & T_0(z_{N-1}) & \dots & T_N(z_{N-1}) \\
0 & \dots & 0 & 0 & \dots & 0 \\
\vdots & \ddots & \vdots & \vdots & \ddots & \vdots \\
0 & \dots & 0 & 0 & \dots & 0
\end{bmatrix}
$$

Appendix B.   Matrix Arising from Collocation Method

B.1   Matrix Arising from Collocation Method

The matrix $[A]$ and $[B]$ from the eigenvalue problem $[A]\boldsymbol{a} = s[B]\boldsymbol{a}$, i.e. (3.22), is shown in the following pages; both are complex squire matrix of order $4N + 4$. The eight boundary conditions are implemented on the last eight rows. And let

$$G_j^n = (\mathcal{M} - l^2)T_n\left(z_{c_j}\right),$$

$$T_n'(z_c) = \frac{dT_n(z_c)}{dz_c},$$

the operator $\mathcal{M}$ is as defined in (3.7), but now in the z_c coordinate

$$\mathcal{M} = (z_c + 1)^2 \frac{d^2}{dz_c{}^2} + (z_c + 1)\frac{d}{dz_c},$$

while the rest of the symbols remains the same as previously defined.

$[B]_{4N+4,4N+4} =$

$$\begin{bmatrix}
T_1(z_{c_1}) & \cdots & T_N(z_{c_1}) & 0 & \cdots & 0 & 0 & \cdots & 0 & 0 & \cdots & 0 \\
\vdots & \ddots & \vdots & \vdots & \ddots & \vdots & \vdots & \ddots & \vdots & \vdots & \ddots & \vdots \\
T_1(z_{c_{N-1}}) & \cdots & T_N(z_{c_{N-1}}) & 0 & \cdots & 0 & \vdots & \ddots & \vdots & \vdots & \ddots & \vdots \\
0 & \cdots & 0 & G_1^1 & \cdots & G_1^N & \vdots & \ddots & \vdots & \vdots & \ddots & \vdots \\
\vdots & \ddots & \vdots & \vdots & \ddots & \vdots & \vdots & \ddots & \vdots & \vdots & \ddots & \vdots \\
\vdots & \ddots & \vdots & G_{N-1}^1 & \cdots & G_{N-1}^N & 0 & \cdots & 0 & \vdots & \ddots & \vdots \\
\vdots & \ddots & \vdots & 0 & \cdots & 0 & T_1(z_{c_1}) & \cdots & T_N(z_{c_1}) & \vdots & \ddots & \vdots \\
\vdots & \ddots & \vdots & \vdots & \ddots & \vdots & \vdots & \ddots & \vdots & \vdots & \ddots & \vdots \\
\vdots & \ddots & \vdots & \vdots & \ddots & \vdots & T_1(z_{c_{N-1}}) & \cdots & T_N(z_{c_{N-1}}) & \vdots & \ddots & \vdots \\
\vdots & \ddots & \vdots & \vdots & \ddots & \vdots & 0 & \cdots & 0 & \vdots & \ddots & \vdots \\
\vdots & \ddots & \vdots & \vdots & \ddots & \vdots & \vdots & \ddots & \vdots & \vdots & \ddots & \vdots \\
0 & \cdots & 0 & 0 & \cdots & 0 & 0 & \cdots & 0 & 0 & \cdots & 0
\end{bmatrix}$$

$$[A]_{4N+4,4N+4} =$$

$$
\begin{bmatrix}
LaG_1^1 & \cdots & LaG_1^N & -(\mathcal{D}u_e)T_1(z_{c_1}) & \cdots & -(\mathcal{D}u_e)T_N(z_{c_1}) & -l^2RiT_1(z_{c_1}) & \cdots & -l^2RiT_N(z_{c_1}) & 0 & \cdots & 0 & 0 & \cdots & 0 \\
\vdots & \ddots & \vdots & \vdots & \ddots & \vdots & \vdots & \ddots & \vdots & \vdots & & \vdots & \vdots & \ddots & \vdots \\
LaG_{N-1}^1 & \cdots & LaG_{N-1}^N & -(\mathcal{D}u_e)T_1(z_{c_{N-1}}) & \cdots & -(\mathcal{D}u_e)T_N(z_{c_{N-1}}) & -l^2RiT_1(z_{c_{N-1}}) & \cdots & -l^2RiT_N(z_{c_{N-1}}) & 0 & \cdots & 0 & 0 & \cdots & 0 \\
l^2(\mathcal{D}u_s)T_1(z_{c_1}) & \cdots & l^2(\mathcal{D}u_s)T_N(z_{c_1}) & 0 & \cdots & 0 & \tfrac{La}{Pr}G_1^1 & \cdots & \tfrac{La}{Pr}G_1^N & LaG_1^1 & \cdots & LaG_1^N & 0 & \cdots & 0 \\
\vdots & \ddots & \vdots & \vdots & \ddots & \vdots & \vdots & \ddots & \vdots & \vdots & & \vdots & \vdots & \ddots & \vdots \\
l^2(\mathcal{D}u_s)T_1(z_{c_{N-1}}) & \cdots & l^2(\mathcal{D}u_s)T_N(z_{c_{N-1}}) & 0 & \cdots & 0 & \tfrac{La}{Pr}G_{N-1}^1 & \cdots & \tfrac{La}{Pr}G_{N-1}^N & LaG_{N-1}^1 & \cdots & LaG_{N-1}^N & 0 & \cdots & 0 \\
0 & \cdots & 0 & -T_1(z_{c_1}) & \cdots & -T_N(z_{c_1}) & 0 & \cdots & 0 & 0 & \cdots & 0 & 0 & \cdots & -T_1(z_{c_1}) \\
\vdots & & \vdots & \vdots & \ddots & \vdots & \vdots & & \vdots & \vdots & & \vdots & & & \vdots \\
0 & \cdots & 0 & -T_1(z_{c_{N-1}}) & \cdots & -T_N(z_{c_{N-1}}) & 0 & \cdots & 0 & 0 & \cdots & 0 & 0 & \cdots & -T_1(z_{c_{N-1}}) \\
0 & \cdots & 0 & G_1^1 & \cdots & G_1^N & 0 & \cdots & 0 & 0 & \cdots & 0 & 0 & \cdots & 0 \\
\vdots & & \vdots & \vdots & & \vdots & \vdots & & \vdots & & & & & & \vdots \\
0 & \cdots & 0 & G_{N-1}^1 & \cdots & G_{N-1}^N & 0 & \cdots & 0 & 0 & \cdots & 0 & 0 & \cdots & 0 \\
0 & \cdots & 0 & T_0(1) & \cdots & T_N(1) & 0 & \cdots & 0 & 0 & \cdots & 0 & 0 & \cdots & 0 \\
0 & \cdots & 0 & \mathcal{M}T_0(1) & \cdots & \mathcal{M}T_N(1) & 0 & \cdots & 0 & 0 & \cdots & 0 & 0 & \cdots & 0 \\
0 & \cdots & 0 & 0 & \cdots & 0 & T_0(1) & \cdots & T_N(1) & 0 & \cdots & 0 & 0 & \cdots & 0 \\
(z_{c_0}+1)T_1'(1) & \cdots & (z_{c_0}+1)T_N'(1) & T_1'(-1) & \cdots & T_N'(-1) & 0 & \cdots & 0 & 0 & \cdots & 0 & 0 & \cdots & 0 \\
T_1(-1) & \cdots & T_N(-1) & T_1(-1) & \cdots & T_N(-1) & 0 & \cdots & 0 & 0 & \cdots & 0 & 0 & \cdots & 0 \\
0 & \cdots & 0 & 0 & \cdots & 0 & T_1(-1) & \cdots & T_N(-1) & 0 & \cdots & 0 & 0 & \cdots & 0 \\
0 & \cdots & 0 & 0 & \cdots & 0 & 0 & \cdots & 0 & 0 & \cdots & 0 & T_1(-1) & \cdots & T_N(-1)
\end{bmatrix}
$$

52

B.2   Additional Notes On Solving the Generalized Eigenvalue Problem

Initially we used MATLAB to solve this eigenvalue problem using the functions `QZ` and `eig`. In seek of a faster solution, we adapted our code to FORTRAN 90, and the eigenvalue problem is solved using LAPACK subroutine ZGGEV3, which computes the generalized eigenvalues, and the generalized eigenvectors for a pair of complex non-symmetric square matrices ($[A], [B]$) using the QZ-algorithm. The resulting improvement of speed is shown in Table 7, where we have tested the collocation method using MATLAB version 2013b in the windows system and FORTRAN in both windows and Linux system, the Galerkin method is also tested for comparison.

Note that theoretically, we could have solved (2.37)-(2.39) without replacing v; instead, solve u, v, w, θ directly using the same approach, resulting in a generalized eigenvalue problem with a different matrix of the same dimension. However, the cross-differentiation on eliminating π would lead to a third order differential term and would thus be a higher order system than the one we solved, for which is less desirable.

Method (system, code)	Time(s)
Collocation (Linux, FORTRAN)	249.27
Collocation (win7, MATLAB)	461.70
Galerkin (Linux, FORTRAN)	470.24
Collocation (win7, FORTRAN)	647.67

TABLE 7. Computation time comparison between Chebyshev collocation method and Galerkin method. (The amount of time needed to solve for $l = 10 \sim 11$ using $N = 30$.)

Appendix C.　Comparing with Galerkin Method

C.1　*Eigenvalue Convergence Comparison*

Comparison of the most unstable growth rate solved using Chebyshev collocation method and the Galerkin method are briefly compared for four sets of $l = 10.0, 5.0, 0.5, 0.1$ at the reciprocal Langmuir numbers $La^{-1} = 100, 1000, 10000$.

For higher wavenumbers such as $l = 10.0$ in Table 8 and $l = 5.0$ in Table 9, both methods converge to 5 significant digits after $N = 20{\sim}30$, and their results are in agreement. During low wavenumbers such as $l = 0.5, 0.1$ in Table 10 and Table 11, both method are not converging but the Galerkin method depict better results; nevertheless, since the main evaluation points in our current work are located at the higher wavenumber range, the solutions from Chebyshev collocation method are adequate.

10.0	$La^{-1} = 100$		$La^{-1} = 1000$		$La^{-1} = 10000$	
N	collocation	Galerkin	collocation	Galerkin	collocation	Galerkin
10	−0.00001	−0.00001	0.84787	0.84992	0.96318	0.96379
20	−0.00001	−0.00001	0.84980	0.84980	0.96361	0.96364
30	−0.00001	−0.00001	0.84980	0.84980	0.96364	0.96364
40	−0.00001	−0.00001	0.84980	0.84980	0.96364	0.96364
50	−0.00001	−0.00001	0.84980	0.84980	0.96364	0.96364
100	−0.00001	−0.00001	0.84980	0.84980	0.96364	0.96364

TABLE 8. Convergence comparison between Chebyshev collocation method and Galerkin method of the growth rate s_r for the most unstable mode for $l = 10, La^{-1} = 100, 1000, 10000$.

5.0	$La^{-1} = 100$		$La^{-1} = 1000$		$La^{-1} = 10000$	
N	collocation	Galerkin	collocation	Galerkin	collocation	Galerkin
10	0.47014	0.47050	0.76723	0.76761	0.80204	0.80213
20	0.47053	0.47053	0.76758	0.76758	0.80206	0.80207
30	0.47053	0.47053	0.76758	0.76758	0.80207	0.80207
40	0.47053	0.47053	0.76758	0.76758	0.80207	0.80207
50	0.47053	0.47053	0.76758	0.76758	0.80207	0.80207
100	0.47053	0.47053	0.76758	0.76758	0.80207	0.80207

TABLE 9. Convergence comparison between Chebyshev collocation method and Galerkin method of the growth rate s_r for the most unstable mode for $l = 5, La^{-1} = 100, 1000, 10000$.

0.5	$La^{-1} = 100$		$La^{-1} = 1000$		$La^{-1} = 10000$	
N	collocation	Galerkin	collocation	Galerkin	collocation	Galerkin
10	0.127392	0.20563	0.216443	0.22009	0.223763	0.22234
20	0.117049	0.20865	0.209648	0.22203	0.223538	0.22410
30	0.106769	0.20931	0.202199	0.22241	0.222899	0.22444
40	0.097370	0.20964	0.193765	0.22259	0.222251	0.22460
50	0.088947	0.20979	0.183412	0.22267	0.221599	0.22467
100	0.059388	0.21007	0.155156	0.22281	0.218275	0.22478

TABLE 10. Convergence comparison between Chebyshev collocation method and Galerkin method of the growth rate s_r for the most unstable mode for $l = 0.5, La^{-1} = 100, 1000, 10000$.

0.1	$La^{-1} = 100$		$La^{-1} = 1000$		$La^{-1} = 10000$	
N	collocation	Galerkin	collocation	Galerkin	collocation	Galerkin
10	0.001885	0.040467	0.030684	0.048162	0.050294	0.049635
20	0.000000	0.044220	0.022762	0.050139	0.045251	0.051370
30	0.000000	0.045536	0.015984	0.050890	0.036009	0.052035
40	0.000000	0.046337	0.011722	0.051370	0.034235	0.052465
50	0.000000	0.046840	0.009153	0.051674	0.032142	0.052738
100	0.000000	0.048076	0.004735	0.052440	0.021439	0.053427

TABLE 11. Convergence comparison between Chebyshev collocation method and Galerkin method of the growth rate s_r for the most unstable mode for $l = 0.1, La^{-1} = 100, 1000, 10000$.

55

C.2   *Stability Curve Comparison*

The stability curve comparison of collocation method and the Galerkin method are shown in Figure 18, the difference between the two lies in the area where $l < 1$, $La^{-1} < 100$, these were the areas where the solutions had poor convergence for our collocation method, the other parts of the curves indicate good agreement between the two methods.
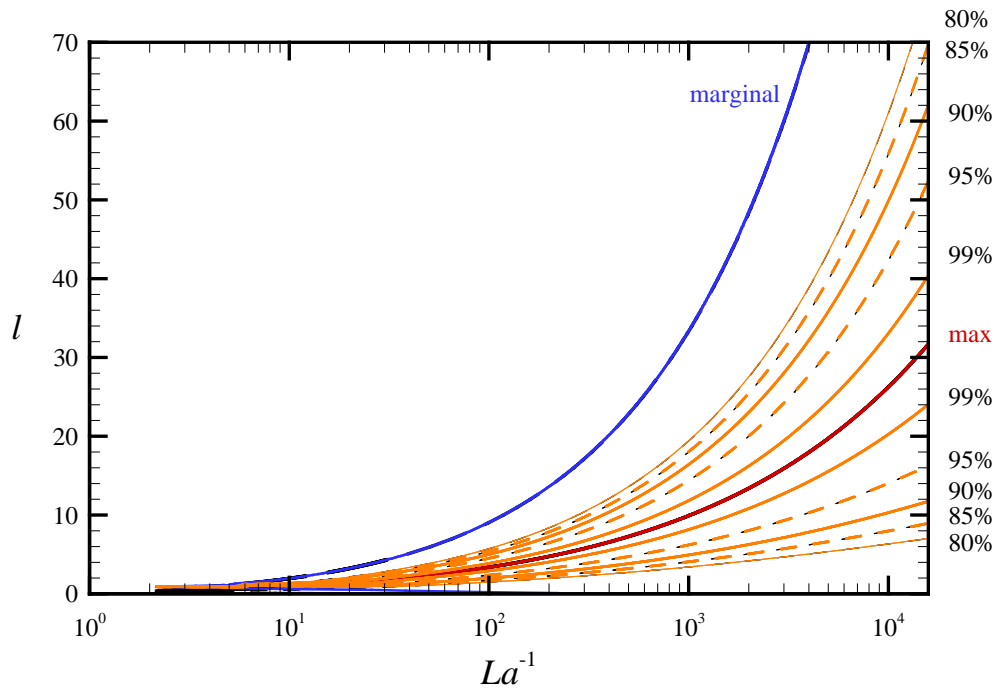

FIGURE 18. Comparison of the curve for collocation method (colored lines) and the Galerkin method (black lines).

C.3 *Growth Rate Comparison*

To further indicate the difference and agreement of the two methods, we have plotted the maximum growth rates on fixed $La^{-1} = 100, 10000$ in Figure 19 and Figure 20. The main difference between the results is in the section where $La^{-1} = 100, l < 1$ this can be seen from Figure 19, where the curves differ in the range $l < 1$, while the rest of the curves fits well. In Figure 20 where $La^{-1} = 10000$, the curves coincide.
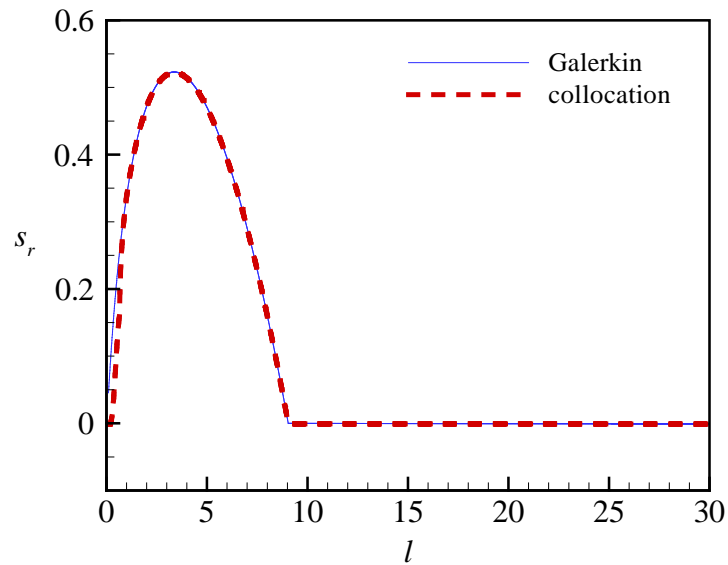

FIGURE 19. Comparison of growth rate between Galerkin (solid lines) and collocation (dashed lines) method for $La^{-1} = 100$ and $N = 30$.
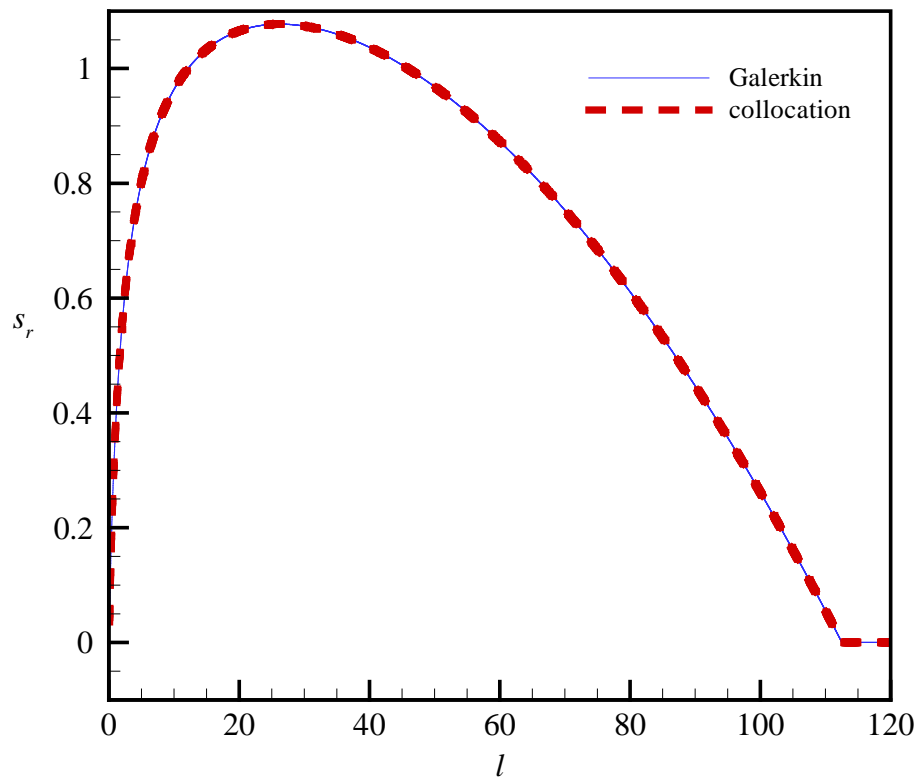
FIGURE 20. Comparison of growth rate between Galerkin (solid lines) and collocation (dashed lines) method for $La^{-1} = 10000$ and $N = 30$.